

INFORMATION TO USERS

This material was produced from a microfilm copy of the original document. While the most advanced technological means to photograph and reproduce this document have been used, the quality is heavily dependent upon the quality of the original submitted.

The following explanation of techniques is provided to help you understand markings or patterns which may appear on this reproduction.

1. The sign or "target" for pages apparently lacking from the document photographed is "Missing Page(s)". If it was possible to obtain the missing page(s) or section, they are spliced into the film along with adjacent pages. This may have necessitated cutting thru an image and duplicating adjacent pages to insure you complete continuity.
2. When an image on the film is obliterated with a large round black mark, it is an indication that the photographer suspected that the copy may have moved during exposure and thus cause a blurred image. You will find a good image of the page in the adjacent frame.
3. When a map, drawing or chart, etc., was part of the material being photographed the photographer followed a definite method in "sectioning" the material. It is customary to begin photoing at the upper left hand corner of a large sheet and to continue photoing from left to right in equal sections with a small overlap. If necessary, sectioning is continued again -- beginning below the first row and continuing on until complete.
4. The majority of users indicate that the textual content is of greatest value, however, a somewhat higher quality reproduction could be made from "photographs" if essential to the understanding of the dissertation. Silver prints of "photographs" may be ordered at additional charge by writing the Order Department, giving the catalog number, title, author and specific pages you wish reproduced.
5. PLEASE NOTE: Some pages may have indistinct print. Filmed as received.

University Microfilms International

300 North Zeeb Road
Ann Arbor, Michigan 48106 USA
St. John's Road, Tyler's Green
High Wycombe, Bucks, England HP10 8HR

77-31,785

HART, Richard Dennis, 1949-
MEASUREMENT OF RADIATIVE MUON
CAPTURE IN CALCIUM.

The College of William and Mary in
Virginia, Ph.D., 1977
Physics, elementary particles and
high energy

University Microfilms International, Ann Arbor, Michigan 48106

MEASUREMENT OF RADIATIVE μ ON CAPTURE IN CALCIUM

A Dissertation

Presented to

The Faculty of the Department of Physics
The College of William and Mary in Virginia

In Partial Fulfillment

Of the Requirements for the Degree of
Doctor of Philosophy

by

Richard Dennis Hart

August 1977

APPROVAL SHEET

This dissertation is submitted in partial fulfillment of
the requirements for the degree of

Doctor of Philosophy

Richard D. Hart

Richard Dennis Hart

Approved, August 1977

Robert T. Siegel

Robert T. Siegel

Morton Eckhause

Morton Eckhause

Franz L. Gross

Franz L. Gross

Rolf G. Winter

Rolf G. Winter

David A. Jenkins

David A. Jenkins
Virginia Polytechnic Institute
and State University

TABLE OF CONTENTS

	Page
ACKNOWLEDGMENTS	v
ABSTRACT	vii
I. INTRODUCTION	1
II. THEORY	3
III. DESCRIPTION OF EXPERIMENT	8
A. Muon and Pion Beams	8
B. Experimental Geometry	9
C. Electronic Logic	11
D. Background	14
E. Calibration of the Timing Logic	18
F. Calibration of the Photon Energy Spectrum	19
IV. DATA ANALYSIS	24
A. Decay Electron Time Spectra	24
B. Calibration for the Photon Asymmetry Measurement	28
C. RMC Photon Asymmetry	31
D. Expression for the Branching Ratio	36
E. Branching Ratio of RMC to MC	41
F. Determination of g_p/g_a	44
V. DISCUSSION AND CONCLUSIONS	48

TABLES	53
APPENDICES	59
REFERENCES	67
FIGURE CAPTIONS	70
FIGURES	74

ACKNOWLEDGMENTS

The author would like to acknowledge the following persons and agencies for their contributions to this work:

Professors Robert T. Siegel, Robert E. Welsh, Morton Eckhause, and John R. Kane, Drs. Colin R. Cox, A. Minick Rushton, and Madhu S. Pandey, and electrical engineer, William F. Vulcan, and graduate research assistant George W. Dodson, for the countless hours which have contributed to this experiment. I am indebted to Professor Robert T. Siegel, my advisor, for the guidance which made my graduate years personally rewarding and extremely enjoyable.

The scintillation counters, precision magnet, and other components of the experimental geometry were designed and built by the William and Mary machine shop under the direction of Mr. Stanley G. Hummel.

Professors Robert T. Siegel, Rolf G. Winter, Franz L. Gross, David A. Jenkins (VPI & SU), John R. Kane, and especially Morton Eckhause, for their critical readings of this manuscript.

Professor Harold W. Fearing, University of British Columbia, for several interesting conversations about radiative muon capture.

Professor H. P. C. Rood, University of Groningen, Institute for Theoretical Physics, for a copy of the program to compute observables in radiative muon capture.

Dr. R. Cohen of Nevis Laboratories for lending us the yoke
for the precision magnet.

My wife, Sharon Louise, for typing the initial draft of this
manuscript.

Ms. Sylvia Stout, for typing the final draft of this manu-
script.

This work was supported in part by the National Science
Foundation.

ABSTRACT

Approximately 1200 background-subtracted photons of energies ≥ 63.5 MeV emanating from the capture of precessing muons by protons in calcium nuclei were observed. From the precession frequency of the muon spin, a value of $+0.90 \pm 0.50$ for the radiative capture photon momentum-muon spin asymmetry was extracted. The photon energy distribution is consistent with an integrated branching ratio of radiative to normal muon capture above 57 MeV of $(21.1 \pm 0.6) \times 10^{-6}$. From a comparison of the photon energy distribution to the predicted results of the theory of Rood, Yano, and Yano, the magnitude of the induced pseudoscalar coupling constant g_p was determined to be $(6.7 \pm 1.5)g_a$, where g_a is the axial vector coupling constant.

The result for the photon asymmetry is in good agreement with a value of about +0.75 predicted by Rood, Yano, and Yano but in disagreement with a previous measurement which gave a slightly negative value for the asymmetry. The result for g_p is in agreement with the value of $g_p \approx +7g_a$ predicted by the Goldberger-Treiman relation. The measured branching ratio is not in good agreement with previous experimental results.

RICHARD DENNIS HART

DEPARTMENT OF PHYSICS

THE COLLEGE OF WILLIAM AND MARY IN VIRGINIA

MEASUREMENT OF RADIATIVE MUON CAPTURE IN CALCIUM

I. INTRODUCTION

The universal Fermi interaction (UFI) is assumed to describe the weak interactions of particles through a vector-minus-axial vector coupling of the weak currents.^{1,2}

Of interest is the strength of the induced pseudoscalar coupling constant g_p in the weak interaction process of muon capture by a proton $\mu^- p \rightarrow n \nu_\mu$. The predicted³ rate of muon capture by a "free" proton depends on g_p directly. A determination of g_p from an experimental measurement of the capture rate can be compared to the theoretical value⁴ $g_p \cong +7g_a$, where g_a is the axial vector coupling constant. While the computation of the capture rates for gaseous and liquid hydrogen targets is complicated by molecular and atomic processes,³ these effects are treatable and earlier experimental results gave³ $g_p = (10.0 \pm 1.6)g_a$. For the description of the process of muon capture by a proton in a complex nucleus of charge Ze , where $Z \geq 2$, much greater theoretical uncertainties arise from the imprecise knowledge of the nuclear states and of the nucleon-nucleon correlation effects³ such as meson exchange.

For ordinary muon capture in a complex nucleus $\mu^- A(Z, N) \rightarrow \nu_\mu B(Z-1, N+1)^*$ the Coulomb attraction between the muon and the nuclear protons concentrates the muon wave function in the nuclear volume, enhancing the capture rate. As a specific example, the capture rate in calcium is about 3500 times the capture rate in hydrogen.

We have studied the photon in the rarer process of radiative muon capture in calcium $\mu^- {}^{40}\text{Ca} \rightarrow \nu_{\mu} {}^{40}\text{K}^* + \gamma$ to gain some insight into the strength of the pseudoscalar coupling when the proton is inside a complex nucleus. The photon is emitted by the mechanism of inner bremsstrahlung and is introduced by attaching an external photon line at all possible places in the muon capture Feynman diagrams. Theoretical studies⁵⁻¹⁰ predict that the approximate rate of radiative to normal muon capture in any element is about $\frac{\alpha}{12\pi} \cong 2 \times 10^{-4}$.

II. THEORY

Radiative muon capture (RMC) was investigated theoretically by Huang, Yang, and Lee⁵ in a study of possible parity violating effects associated with muon capture by a free proton. They showed that the (V-A) structure of the weak interaction dictated that photons emitted by the muon have an angular dependence $P(\theta) = 1 + \alpha \cos \theta$, where $\alpha = +1.0$ and θ is the angle between the photon momentum and the muon spin direction. This corresponds to a maximal parity violating effect.

In a study of ordinary muon capture (MC), Primakoff⁶ introduced the pseudoscalar and weak magnetism couplings into the theoretical computation of the capture rate by keeping nucleon recoil terms in a nonrelativistic effective Hamiltonian. The evaluation of the nuclear matrix elements by the closure approximation is presented and the importance of the exclusion principle in inhibiting the availability of the final nuclear states of a complex nucleus is discussed. The extension of the closure approximation and the retention of the induced terms in the calculation of the RMC rate which was derived by Cantwell⁷ is presented.

Bernstein⁸ and, separately, Manacher⁹ examined the contributions of the induced terms to the RMC rate. They predicted an enhancement of the radiative rate by about 30% at the high energy end of the photon spectrum due to radiation from the pion, proton, and anomalous

magnetic moments of the nucleons. Bernstein⁸ further showed that much of this radiation decreases the overall photon asymmetry. Thus, the strength of g_p can be inferred by measuring the rate of photon emission and the deviation of the photon asymmetry from the value of +1.0.

An exhaustive theoretical study of RMC in medium Z nuclei is that of Rood and Tolhoek¹⁰ (henceforth, RT). Contributions to the RMC rate from the virtual pion, proton, muon, and anomalous magnetic moments of the nucleons is considered in their theory. By using several nuclear models and examining the ratio of the computed radiative to the normal muon capture rate of each model, they conclude that systematic uncertainties from the incomplete knowledge of the nuclear physics probably tend to cancel in the ratio of computed matrix elements, so that the calculated branching ratio of RMC to MC is reliable to about 10%. Their final results were computed using a shell model description of the nuclear states and applying the closure approximation in the reduction of the nuclear matrix elements (denoted as the closure harmonic oscillator or CHO model).

The results of several previous experiments^{11,12} have been compared to the theoretical predictions¹⁰ of RT. In addition, several later theories^{13,14,15} of RMC include a comparison of predictions to those of RT¹⁰. Thus, the RT theory¹⁰ is a "common denominator" of much of the past work on RMC so that we have analyzed our data with respect to this theory to enable a comparative study of our results with both theoretical and earlier experimental work.

The most recent theoretical effort is that of Rood, Yano, and Yano¹³ (henceforth, RYY). They treat the non-local effects in the radiative capture process, which arise since the photon emission and the weak interaction take place at different points in space-time, by using a formalism developed by Martin and Glauber¹⁶ to study radiative K electron capture. For diagrams in which the muon radiates a photon, the intermediate state muon is described by the propagator of a muon in the field of a spherical nuclear charge distribution. For all other diagrams (Fig. 1), the pion and proton propagate as free particles. Their predicted RMC rate is about 24% lower than that predicted¹⁰ by RT in the high-energy end of the photon spectrum. Further, the contribution of the proton radiation is relatively more suppressed than that of the muon so that the net asymmetry of these photons is increased by about 3% from the value of +0.75 predicted¹⁰ by RT. It was thought¹⁷ that the inclusion of the pion propagator would affect the normal muon capture rate since capture could now take place outside the nucleus. However, any such effect is apparently small¹⁸ so that the MC rate is computed, as in the theory¹⁰ of RT, in a manner consistent with the CHO calculations of Luyten, Rood, and Tolhoek¹⁹. Our result for the magnitude of the induced pseudoscalar coupling constant was determined from the comparison of the predictions of the RYY¹³ theory to our experimental data.

Fearing¹⁴ extended a deterministic approach, first used by Foldy and Walecka²⁰ in the computation of normal muon capture rates, to

include radiative muon capture as well. Experimental photoabsorption cross sections are related to the contribution of the nuclear dipole resonance to muon capture. The expression "dipole" denotes the dipole component of a multipole expansion of the nuclear matrix element. The other multipole terms are evaluated in accord with the CHO model¹⁰ of RT. It is claimed that, for the same values of the coupling constants, the branching ratio of RMC to MC in ^{40}Ca is reduced by about 20% with respect to the predicted¹⁰ result of RT. However, this claim has been disputed by Rosenstein¹².

Borchi and de Gennero¹⁵ applied a phenomenological approach to nuclear structure, known as the Migdal²¹ theory, to RMC and MC. In this model, the nucleus is defined as a system of interacting quasi-particles whose motions are described by Green's functions. Free parameters of the theory are adjusted to reproduce known properties of nuclei and to predict new ones. Both the radiative and normal muon capture rates in ^{40}Ca are computed to be about 40% lower than the calculated rates¹⁰ of RT. The branching ratio, then, remains the same as that predicted¹⁰ by RT. This supports the RT claim that their results are independent of the choice of nuclear model. The prediction of Borchi and deGennero¹⁵ for the photon asymmetry is the same as that predicted¹⁰ by RT at the lower energy end of the photon spectrum but the asymmetry is relatively increased by about 10% at the high energy end of the spectrum. It is probably the case that the computations of Borchi and deGennero¹⁵ do not take into account all of the non-local effects in the radiative capture process.

Fearing²² has given a concise account of the photon momentum-muon spin asymmetry summarized in a general theorem. He cautions that neglected terms in the radiative capture process may effect the value of the photon asymmetry since they are second-order corrections to the branching ratio but first-order corrections to the photon asymmetry.

III. DESCRIPTION OF THE EXPERIMENT

A. Muon and Pion Beams

The Space Radiation Effects Laboratory²³ synchrocyclotron was operated on a 19 millisecond pulsed cycle with a duty factor of about 50%.

During each machine cycle the proton beam is accelerated to 600 MeV and brought to a coasting orbit where π^{\pm} are produced by proton collisions on a carbon filament internal target (Fig. 2). The fringing field of the cyclotron main magnet directs pions of the desired charge and momentum to the A and B quadrupole lenses which focus the beam, causing it to enter a corridor of 22 containment quadrupoles called the muon channel.

A negative muon beam develops as a number of the π^{-} undergo weak decay in flight. The decay is isotropic in the pion rest frame but angular momentum conservation and the right-handed helicity of the final-state antineutrino give rise to muons totally longitudinally polarized. The beam which emerges from the muon channel is composed of pions, a higher momentum "forward" muon beam partially polarized in the downstream direction (along the muon momentum in the laboratory frame) and a lower momentum (85 MeV/c) "backward" muon beam with partial polarization pointing upstream.

The desired beam component is momentum-selected at the muon channel dipole magnet and enters the upstream and downstream quadrupoles for final focusing before emerging into the experimental area at a height of 137 cm from the floor.

Reversal of the polarity of all the magnets results in a π^+ and μ^+ beam generated with momentum and, for the muon, a magnitude of the muon spin polarization, identical to the π^- and μ^- beams. The forward μ^- and μ^+ beams were not used and henceforth "muon beam" will refer to the "backward" μ^- beam.

B. Experimental Geometry

A direct measurement indicated that 75% of the muon beam which emerged from the 35cm x 35cm aperture in the downstream quadrupole (Fig. 3) passed through a 15cm wide by 20cm high opening in a wall of borated polyethylene and concrete designed to absorb most neutrons produced by the interactions of μ^- which stopped in the quadrupole and reduce the overall background due to beam-associated events. Downstream of counter 1, the shielding for the NaI detector was composed of lead since the 74 nsec lifetime²⁴ of a μ^- stopped in lead is short in comparison with a protection time interval of 1000 nsec which was imposed by the electronic logic.

The beam was monitored by four plastic scintillants and a plastic Cerenkov counter as shown in Fig. 3.

Targets were held within counter 4 centered along the beam line in the 15cm gap between 25cm x 25cm pole tips of the precession

magnet. In this geometry, the beam line, precession magnet field, and the NaI axis were mutually orthogonal. The residual polarization of a stopped muon pointed upstream (towards counter 1) and subsequently precessed in the plane defined by the beam line and NaI axis.

The seven NaI photomultiplier tubes were enclosed by a double ring of soft iron cylinders to shield them from the magnetic field. The pulse height response of the NaI to the 1.33 MeV line of a ^{60}Co source showed no visible gain shift in a precession field on/off test. In order to lessen the systematic effects due to the presence of the field, the magnet was on throughout the entire experiment. The non-uniformity of the field throughout the target volume was measured to be less than 1.3% at an average field strength of 537.6 gauss. The magnet was driven by a DC power supply monitored during each run by observing the coil voltage and the voltage across a shunt in the power supply.

To insure a constant solid angle (defined by the positioning of the target and counter 8), Mylar tape on the magnet pole tips outlined the positioning of counter 4, which supported the target, and the orientation of counter 8 was fixed by its insertion into a slotted sheet of lead which was capped over the NaI and rested on the outer iron ring.

Photon and electron events were identified by a counter hodoscope consisting of four plastic scintillants, a plastic \checkmark Cerenkov counter, and a NaI(Tl) detector (Fig. 3).

C. Electronic Logic

A calcium target (97% ^{40}Ca natural abundance) measuring $12.5 \times 17.5 \times 1.88\text{cm}^3$ was tilted at 45° to the vertical to present an effective target $12.5 \times 12.5 \times 2.5\text{cm}^3$ (3.9 gm/cm^2) to the beam. The beam entered the target after passing through counter 3, which was constructed as a $12.5\text{cm} \times 17.5\text{cm} \times 0.157\text{cm}$ plastic scintillant optically coupled to the target side of a thin slab of Lucite to minimize the contribution of the material of this counter to the stop rate. Anticoincidence counter 4 surrounded the remaining exposed target so that a muon stop in the target was defined by a $1.2 \cdot \bar{C}1 \cdot 3 \cdot \bar{4}$ coincidence.

To insure that the recorded time distribution of the events was unambiguous, stop coincidences were "cleaned", i.e., rejected, if another beam particle arrived in the experimental area, as evidenced by a second 1.2 coincidence, within $\pm 1 \mu\text{sec}$ (about three muon lifetimes in calcium), as shown in Fig. 4.

Since the branching ratio is ultimately expressed as a ratio of the number of photons to electrons recorded, the logic protection circuits described below were designed for both photon and electron events in order that systematic effects in the analysis would cancel.

Event signatures and photon-neutron discrimination. Photons which converted in a 0.30cm lead sheet sandwiched between counters 6 and 7 were identified by a $\overline{5,6} \cdot 7 \cdot C2 \cdot 8$ coincidence (Fig. 5). An electron signature was $5 \cdot 6 \cdot 7 \cdot C2 \cdot 8$. Both types of events produced relativistic

particles so that Cerenkov counter C2 provided identification as well as discrimination against possible neutron-induced proton knockout events in the counters or lead sheet.

Pion Protection. Prompt photons from a small beam contamination of pions were vetoed by a fast $\overline{1,2}$ in anticoincidence with $7 \cdot C2 \cdot 8$ coincidences.

Carbon decay electron contamination. A similar $\overline{3}$ anticoincidence with a $7 \cdot C2 \cdot 8$ coincidence lessened the probability of detection of decay electrons from muon stops in this counter.

Pile-up protection. The long relaxation time constant of the NaI(Tl), which necessitates integrating the electronic response over an extended time interval, raised the possibility of recording a false high energy photon event because of pulse height addition of a true photon event and a second (undetected) particle entering the NaI. In consideration of this (Fig. 6), the NaI output was first amplified by a factor of 2. One output, used for the energy measurement was further amplified, then integrated and digitized. A second output, used as a timing pulse, was fed into a timing discriminator with a modified AC coupled input. The timing discriminator output pulses were rejected if a second discriminator pulse occurred up to 4 μ sec earlier or up to 1 μ sec later in time. The event detection efficiency and the effectiveness of the pile-up rejection circuit were maximized by setting the timing discriminator threshold just above the noise band of the NaI input pulses.

As a precautionary measure in the event that the pile-up rejection circuit was not as efficient as hoped, photon and electron events were also discarded if a charged particle (in the case of an electron event, a second charged particle) was detected within ± 1 μsec as evidenced by a 5.6 coincidence. However, on removing the second 5.6 "cleaning" but retaining the pile-up protection, no change in the rate of electron events per muon stop was observed, giving a good indication that the pile-up rejection circuit was working efficiently. About 12% of all electron events were rejected by this circuit. The timing discriminator output rate during data collection runs was 1 pulse per 42 μsec .

Pulses from counter 8 constituted the time pickoff of all events. The $\overline{5,6}$ veto was periodically removed from the photon signature to allow each electron event to route as both an electron and photon event. The "photon" scintillant timing pulse was then timed to within ± 1 nsec of the electron timing pulse prior to coincidence with a NaI timing pulse. This procedure insured that the time distributions of the photon and electron events were recorded with respect to the same muon spin phase.

A scintillant event signature in coincidence with a NaI timing pulse produced a time to amplitude converter (TAC) START signal. A delayed muon stop signature constituted the STOP input of the TAC. The TAC itself was gated by a 1500 nsec wide coincidence between a muon stop and an event pulse, constructed so that 600 nsec was available for background events (i.e., events occurring before the actual muon stop signature) and 900 nsec for foreground events.

Both the digitized TAC output and the digitized energy information were processed by the SREL on-line data acquisition system. The electron and photon events were distinguished by routing each to separate 256 channel sectors of the energy analog to digital converter (ADC). The energy and time information of each photon and, due to rate limitations, every other electron event were written to magnetic tape.

Scaler rates for a typical RMC data collection run are displayed in Table 1.

D. Background

The major source of background in the RMC photon spectrum was external bremsstrahlung (henceforth, "bremsstrahlung") produced by the scattering of muon decay electrons in the target. If we use the predicted¹⁰ branching ratio of RMC to MC of about 2.0×10^{-4} to estimate the total number of RMC events observed, it is then deduced that there is about 40 times that number of bremsstrahlung events contaminating the foreground RMC signal. Moreover, the recorded time distribution and asymmetry of the bremsstrahlung spectrum are similar, to within a few percent, of the decay electron data, indicating it originates from the decay electrons of muons bound to calcium nuclei.

In the theoretical study of the electron energy spectrum from bound-muon decay, Huff²⁵ showed that for calcium-like atoms about 3% of the electron momenta exceed the $m_{\mu}/2$ (≈ 53 MeV/c) limiting momentum of free-muon decay electrons, extending up to about 57 MeV/c. If we consider

the broad photon resolution of the NaI detector, it is possible that bremsstrahlung may contaminate the RMC data up to about 65 MeV.

A measurement of the beam-unassociated background, to be discussed momentarily, showed that it was not intense enough to produce the observed background level of either photon or electron events below 63 MeV. The summed foreground and background photon energy spectra of the data collection runs (Fig. 7) are observed to be similar in appearance. This similarity also holds for the foreground and background electron energy spectra, where the foreground spectrum is known to originate from muon decay electrons. We conclude that the majority of the background photon and electron events are beam-associated, and are presumably due to rejected muon stops which produced an event within the background time interval of an accepted muon stop.

An enlarged view of the foreground and background photon energy spectra in the region of the upper limit of the bremsstrahlung is shown in Fig. 8. In the background spectrum a highly populated distribution of bremsstrahlung events below 63 MeV is seen to fall abruptly into a gently sloped distribution of photons of higher energies. The smoother distribution of photon events above 63 MeV observed in the foreground spectrum corresponds to the presence of the RMC signal. From this study, a lower limit of 63.5 MeV for accepting RMC events for analysis was chosen. However, a careful examination of the foreground distribution of photon events shows an inflection between 63.5 MeV and 64.5 MeV which bears consideration and will be discussed further.

With the cyclotron off, the beam-independent background was measured by using a pulse generator to simulate stop coincidences with the remainder of the electronic logic operating as usual. The data accumulated with the beam off is displayed in Fig. 9. We believe the beam-off electron energy spectrum to represent charged showers which traversed the NaI at all possible entering angles consistent with the counter geometry. As ascertained from the scaler readings, 99% of the beam-off electron scintillant signatures were accompanied with a coincident NaI timing pulse. This assures that the 100 nsec duration of the NaI timing pulse was wide enough. If the remaining 1% of events were either of insufficient energy to produce a timing pulse or were rejected by the NaI pile-up logic, then the NaI detection efficiency was greater than 99% throughout the entire energy scale.

The background level of the RMC photon data between 63.5 MeV and 89.5 MeV was observed to be 1.38 ± 0.08 events/channel. The recorded number of beam-off events (for the same number of simulated stops) in the same energy interval results in 0.78 ± 0.05 events/channel or about 57% of the observed rate. We note the similarity of the slopes in the beam-on and beam-off background photon energy spectra between 63 and 90 MeV (Figs. 8 and 9).

The photon energy scale was calibrated by observing prompt photons from pions captured on protons. During a special set of these runs, the converter thickness was successively diminished in order to measure the relative number of photons per pion capture per cm of lead

converter. From the data of these runs (Fig. 10) it is clear that the photon signal decreases linearly with decreasing converter thickness and no discernible signal is observed with the converter removed.

About 3% of the total beam time was devoted to runs with the converter removed. A comparison with the 0.30cm "converter-on" runs showed a reduction in the number of background-subtracted photon events below 63 MeV by a factor of 10. Events in the "converter-out" photon spectrum between 63 and 90 MeV were equally distributed between the foreground and background time channels and occurred with an intensity (after normalizing to the "converter-in" recorded muon stops) of 0.7 ± 0.2 events/channel or about 51% of the "converter-in" background rate. It is not possible to determine from the data if this contribution to the background rate persisted with the converter was in place.

Finally, there appeared in all the time spectra (both electron and photon, and for any chosen energy interval) a contamination of unknown origin in the form of an $\approx 10\%$ excess number of events in the first 80 time channels of the foreground spectrum immediately following the prompt time channel. This noise was well contained inasmuch as it terminated rapidly and completely as determined by fitting the time spectra well beyond the contamination, extrapolating the fitted spectrum into the contaminated region, and subtracting the fitted spectrum from the data. The data in the contaminated region was not used in any phase of the analysis.

E. Calibration of the Timing Logic

TAC Calibration. With the beam off, coincidences between a 10 MHz pulse train output from a time mark generator (TMG) and the discriminated pulses of counter 1 responding to a radioactive source formed the TAC START signal. The slow 100 KHz TMG trigger formed the TAC STOP signal so that the measured time intervals Δt were

$$\Delta t = \frac{\text{integer}}{10 \text{ MHz}} = 100 \text{ nsec}, 200 \text{ nsec}, \dots$$

Two calibrations of the TAC gain, of 1.75 nsec/channel and 1.70 nsec/channel, were obtained. The latter calibration, performed at the end of the experiment, was used throughout the analysis, so that a systematic error of 2.8% was attached to the measured value of the total muon lifetime in calcium because of the variation in calibration results.

It was possible to check each data run for anomalous or long-range drifts in the TAC gain by using as a relative monitor the muon spin precession frequency determined from the decay electron time spectra. The precession frequency should not vary since the precession magnet field strength was constant. It was found that, except for a small number of consecutive runs, the muon spin precession rate was constant throughout the experiment. The data from the group of runs inconsistent with the majority gave relative values of both the muon spin precession frequency and muon lifetime in calcium higher by about 8%. However, the data from these runs were accepted for analysis and in so

doing (a) shifted the final values of the measured lifetime and precession frequency by about 1.4% upward and (b) contributed to a slight "washing out" of the recorded asymmetry of both photons and electrons when the time spectra of all data runs were summed together. This will be discussed later.

Linearity. To test the TAC for linearity, a high rate of time-independent signals was necessary and thus the TAC START was replaced by a (5,6) singles pulse. The beam remained off during this time and no radioactive sources were employed. The test indicated some pile-up in the TAC channels below 160. Consequently, what little data existed below channel 180 was not included in the analysis.

Resolution. The timing resolution was determined from the time spectrum of photons from pions stopped in a LiH target as taken during each photon energy calibration run. A typical timing spectrum (Fig. 11) fit to a Gaussian distribution indicated 4 nsec full width at half maximum (FWHM).

F. Calibration of the Photon Energy Spectrum

Periodic calibration of the photon spectrometer was done by observing the prompt photons from the processes:



which materialized in the 0.30cm lead converter.

In (1) the photon is monoenergetic with energy 129.4 MeV. In (2) observation of either photon gives a flat distribution of photon energies from 55 MeV to 83 MeV due to Doppler shifting as a result of the residual energy of the π^0 .

The muon channel dipole magnet was set to select the 200 MeV/c pion beam and the degrader increased to 10cm of borated polyethylene and 17.5cm of graphite to stop most pions in a plate of LiH or Li used in place of the calcium target. The $\overline{1,2,3}$ veto was removed from the photon signature to allow observation of the prompt photon events.

The prompt photon energy spectrum of π^- in Li was normalized and subtracted from the photon energy spectrum of π^- in LiH in accordance with the results of Chabre et al.²⁶ to give the photon energy spectrum from processes (1) and (2) above (Fig. 12).

The absolute detection efficiency for photons could not be determined from the π^- (LiH-Li) calibration runs due to an uncertainty in the actual number of pion stops in the target. Moreover, the data from these runs could not easily be used to determine the energy dependence of the conversion probability of photons in the lead sheet. Instead, the photon detection efficiency versus photon energy was computed by a Monte Carlo simulation of the passage of photons through the experimental geometry, as discussed in Appendix 1.

Also displayed in Fig. 12 is the result of a Monte Carlo calculation of the NaI energy spectrum corresponding to processes (1) and (2). The statistics of the Monte Carlo result have been removed

by curve smoothing. The assumed gain of the NaI energy scale used in the calculation was 0.511 MeV/channel. By coincidence, this is very nearly the determined gain of the experimental NaI energy scale so that the two spectra in Fig. 12 can be compared directly. Reasonable agreement is seen. The computed absolute photon detection efficiency versus primary photon energy is displayed in Fig. 13. A 0.30 cm Pb converter is assumed in position.

The electronic response of the NaI to 129.4 MeV photons which materialized in the converter can be noted in the higher energy peak of Fig. 14. We note from Fig. 10 that the separation between the upper (129.4 MeV) peak and the lower (55-83 MeV) peak worsens with increasing converter thickness, indicating that the converted photon pair suffers interactions (scattering, ionization, bremsstrahlung) in the lead sheet and counters 7, C2, and 8. Thus, the residual energy of the pair entering the NaI is not a priori monoenergetic for each 129.4 MeV event recorded.

Pondrom and Strelzoff²⁷ showed that the electronic response, or resolution function, of a NaI detector to monoenergetic events of energy E_{true} can be re-expressed as a function $R(p)$, where p is the ratio of energy E_{measured} to E_{true} . They further showed that $R(p)$ is the same whether constructed from the resolution function of monoenergetic events of energy E_{true} or from a resolution function of an energy different from E_{true} . We can construct $R(p)$ from the expressions:

$$R(p) = \frac{\text{data}(I)}{\text{data}(I_p^{129.4})}, \quad \text{with}$$

$$p = \frac{129.4 \text{ MeV} + (I - I_p^{129.4})M}{129.4 \text{ MeV}} = \frac{E_{\text{measured}}}{E_{\text{true}}}.$$

In these expressions $\text{data}(I)$ denotes the number of 129.4 MeV events observed in the I th NaI channel, $I_p^{129.4}$ denotes the peak channel of the 129.4 MeV distribution of events, and M is the gain of the NaI energy scale in MeV/channel. An exponential function was used to approximate the number of 129.4 MeV events below channel 145 which could not be separated from the distribution of events in the lower energy peak. $\text{Data}(I)$ is given for $I \geq 145$ by the data in Fig. 14 and $\text{data}(I) = \text{data}(145) \exp((I-145)/\lambda)$ for $1 \leq I \leq 144$. The parameters $I_p^{129.4}$, M , and λ must be determined.

The resolution function for all photon energies between 55 and 83 MeV were constructed from $R(p)$. These constructions introduced two parameters: the assumed peak channel position I_p^{55} of the 55 MeV resolution function and the assumed peak channel position I_p^{83} of the 83 MeV resolution function, which were then used to extrapolate linearly the peak channels of the other resolution functions. Each of the resolution functions (from 55 to 83 MeV) was normalized to its corresponding absolute photon detection efficiency. All the resolution functions between 55 and 83 MeV were then summed together, channel-for-channel, and the resultant spectrum normalized to the same total number of events in the lower energy peak of Fig. 14 (after subtracting from

this distribution the exponential tail below channel 145 of the 129.4 MeV distribution). The χ^2 of the fit was then computed. The variables were adjusted until a best-fit to the lower energy peak was obtained (Fig. 14, darkened circles).

The best-fit values of the variables were:

$$M = 0.51 \text{ MeV/channel}$$

$$\lambda = 45.5 \text{ channels}$$

$$I_p^{129.4} = \text{channel } 194$$

$$I_p^{83} = \text{channel } 124$$

$$I_p^{55} = \text{channel } 77$$

$$\chi^2/\text{fitted channel} = 1.016$$

The function $R(p)$ is displayed in Fig. 15. Resolution functions for photons of several energies are displayed in Fig. 16. Both figures represent smooth curves drawn through the true resolution functions.

IV. DATA ANALYSIS

A. Decay Electron Time Spectra

If we assume a muon is bound at $t = 0$ to a calcium nucleus in the calcium target, the probability of observing a decay electron in the time interval t to $t + dt$ at an angle ϕ with respect to the muon spin is:

$$I(t) = \exp(-t/\tau_{Ca}) \Lambda_{Decay}^{Ca} (1 + P\alpha_e \cos \phi) dt \quad (3)$$

where

τ_{Ca} is the lifetime of a bound muon to a calcium nucleus,

Λ_{Decay}^{Ca} is the decay rate of a muon bound to a calcium nucleus (taken from Huff²⁵ to be $(99 \pm 1)\%$ of the free muon decay rate),

P is the magnitude of the residual muon polarization in the ground state muonic atom and is given by the magnitude of the beam polarization P_B multiplied by the polarization factor D_{Ca} in calcium

α_e is the average asymmetry of the decay electron momenta with respect to the muon spin of all recorded electron events, and

$\phi = \omega t + \phi_0$ is the angle between the muon spin and the time pickoff counter 8; ω is the spin precession rate and ϕ_0 the spin phase at $t = 0$.

We take dt to be the time channel width of 1.70 nsec. We then generalize to the case of N muons and define the variables A and S_{Ca} as: $A = N \Lambda_{Decay}^{Ca} \times (1.70) \text{ channel}^{-1}$ and $S_{Ca} = P\alpha_e$ (dimensionless). We replace the phase ϕ_0 with $\phi_0 - \pi/2$. If we make these changes in Eq. (3), $I(t)$ defines the number of decay electrons originating from muons bound to calcium nuclei observed in the time channel of time coordinate t (ignoring geometrical factors)

$$I(t) = A \exp(-t/\tau_{Ca})(1 + S_{Ca} \sin(\omega t + \phi_0))$$

To this $I(t)$ we add a term for those decay electrons originating from muons bound to carbon nuclei (scintillants 3 and 4) and a term for the background G per channel as determined from the background time ($t < 0$) distribution. We finally obtain

$$I(t) = A \exp(-t/\tau_{Ca})(1 + S_{Ca} \sin(\omega t + \phi_0)) + \quad (4)$$

$$B \exp(-t/\tau_C)(1 + S_{sc} \sin(\omega t + \phi_0)) + G,$$

where

τ_C (=2034 nsec) is the lifetime of a muon bound to a carbon nucleus²⁴ and

$S_{sc} = (P_B \cdot D_{sc} \cdot \alpha_e)$, where D_{sc} is the polarization factor in scintillant.

S_{sc} was eliminated as an independent variable by using the combined results of Sundelin et al.²⁸ and Anderson²⁹ ($D_{Ca}/D_{Carbon} = 0.70 \pm 0.02$) and Buckle et al.³⁰ ($D_{Sc}/D_{Carbon} = 0.33$), to obtain $S_{sc} = S_{Ca}/2.12$. The foreground decay electron time distribution (Fig. 17a) in the time interval from 137.7 nsec through 783.7 nsec from $t = 0$ of each RMC data run was least-squares fitted to the time distribution function $I(t)$ with A , τ_{Ca} , S_{Ca} , ω , ϕ_0 and B variable.

The normalized χ^2 of the best fits to the 63 individual spectra were distributed about 1.0 with 90% of the χ^2 lying within the interval $0.9 \leq \chi^2 \leq 1.1$. The combined results of the individual fits gave

$$\tau_{Ca} = (366 \pm 8) \text{ nsec}$$

$$S_{Ca} = 0.0457 \pm 0.0005$$

$$\omega = (0.04689 \pm 0.00007) \text{ radians/sec}$$

$$\phi_0 = (1.63 \pm 0.02) \text{ radians}$$

$$B/A = (2.3 \pm 0.2)\%$$

$$G/A = 7.9\%$$

The error associated with τ_{Ca} is due, for the most part, to the systematic error attached to the TAC calibration.

From the sum of the individual electron time spectra we obtained:

$$\tau_{Ca} = 365.7 \text{ nsec}$$

$$S_{Ca} = 0.04116$$

$$\omega = 0.04673 \text{ radians/nsec}$$

$$\phi_0 = 1.631 \text{ radians}$$

with errors similar to those above. A comparison of the results of the summed data to the results of the individual fits showed that the asymmetry parameter S_{Ca} was reduced 11% by summing the data prior to fitting. This decrease was due to variations in the prompt channel ($t = 0$) of the time spectra accumulated during the first weeks of the experiment and slight variations of the precession frequency observed in some of the runs. A correction for this "washing out" of the asymmetry will be applied in the analysis of the RMC time spectra.

The result for τ_{Ca} is in poor agreement with previous measurements,^{11,12,31} which tend to give $\tau_{Ca} \sim 336$ nsec. Consequently, the discrepancy was investigated carefully.

For a fixed precession field strength, the measured muon spin precession frequency ω can be used as a check of the TAC gain. The measured field strength was 537.6 ± 20.0 gauss (the error represents the uncertainty in the calibration of the Hall probe) from which ω was computed to be (0.0457 ± 0.0017) radians/nsec and thus in good agreement with the measured value of 0.0469 radians/nsec.

In another check we analyzed the positron time spectrum accumulated in several runs of μ^+ in calcium from which the measured μ^+

lifetime was 2231.0 ± 88.0 nsec, in agreement with the most recent measurement³² of about 2197.0 nsec.

Our measurement of τ_{Ca} gives for the capture rate of muons bound in calcium ($\Lambda_{Cap}^{Ca} = \tau_{Ca}^{-1} - \Lambda_{Decay}^{Ca}$):

$$\Lambda_{Cap}^{Ca} = (22.85 \pm 0.62) \times 10^5 \text{ sec}^{-1}$$

This capture rate entered directly into the determination of the branching ratio. Use of this result for the capture rate admits an overestimate of the branching ratio by as much as 8.6% if one elects instead to use $\tau_{Ca} \approx 336$ nsec.

B. Calibration for the Photon Asymmetry Measurement

The magnitude of the sinusoidal oscillation S_{Ca} observed in the time spectrum of the summed electron data can be expressed as:

$$S_{Ca} = P\alpha_e \times (1.11)^{-1} \quad (5)$$

The factor of 1.11 is a necessary correction in view of the reduction of the measured asymmetry parameter S_{Ca} by a factor of 11% resulting from summing the data prior to analysis.

A recent measurement³³ of the SREL muon beam polarization gave $P_B \approx 0.62$. From a theoretical³⁴ study which predicts $D_{Ca} \sim 1/6$ one would anticipate that $P \approx 0.62 \times 1/6 \approx 0.10$.

Johnson et al.³⁵ have shown that the average electron momentum-muon spin asymmetry of all decay electrons from muons bound to ^{40}Ca

nuclei differs by less than 1% from the value of 1/3 for the average electron asymmetry of free muon decay. However, the simple prescription $S_{Ca} = 1/3 Px(1.11)^{-1}$ is invalid since the lead converter, as well as the target and counters, have high efficiency for stopping low energy electrons. The effect of the presence of the lead converter was measured by running μ^- in calcium with the converter removed.

From a comparison of the electron time spectra of 0.30cm "converter-in" versus "converter-out" runs, a reduction of μ -e events per μ -stop by 2.02 ± 0.04 due to the presence of the converter was observed. This result was used as a consistency check of a Monte Carlo calculation of the detection efficiency of the bound muon decay electron energy spectrum³⁵ (Appendix 1). The Monte Carlo results of the NaI electron energy spectrum for 0.30cm "converter-in" and "converter-out" are displayed in Fig. 18a and are compared to the experimental 0.30cm "converter-in" and "converter-out" electron energy spectra, shown in Fig. 18b. The agreement between the simulated and experimental spectra is good. The absolute detection efficiency for the electron energy spectrum was computed to be 0.829 ("out"), 0.485 ("in"), and 1.71 for their ratio. It was determined from a "converter-in" run with the NaI pile-up rejection circuit removed that 5% of the electron scintillant signatures were due to electrons of insufficient energy to produce a timing pulse in the NaI. Examination of the simulated energy spectrum then imposes an electronic threshold of the timing discriminator at 3 MeV. From this, the computed efficiencies were 0.788 ("out"),

0.441 ("in"), and 1.8 for their ratio. A ratio of 2.0, in agreement with experiment, is obtained if one assumed a 6.6 MeV electronic threshold for detecting electrons.

The V-A theory of free muon decay was used to determine the electron momentum-muon spin asymmetry dependence of the bound decay electron energy spectrum. By recording the asymmetry of each event in the Monte Carlo program, it was possible to determine the average asymmetry of all electron events, as well as the average asymmetry α_e^{MC} of all electron events above an arbitrary energy cut-off. We also measured, from Eq. (4), values of S_{Ca} for the summed electron data as a function of lower NaI channel cut-off.

In a comparison of S_{Ca} with the electron asymmetry α_e^{MC} determined by the Monte Carlo program, three reasonable calibrations were chosen and we used expression (5) to calculate P

$$P = \frac{S_{Ca} \times 1.11}{\text{computed electron asymmetry}} = \frac{S_{Ca} \times 1.11}{\alpha_e^{MC}}$$

The calibrations were:

- (a) an assumed electronic threshold of 3 MeV, which gave

$$P = \frac{(0.0411 \pm 0.0005) \times 1.11}{0.4164} = 0.110 \pm 0.001$$

- (b) an assumed electronic threshold of 6.6 MeV, which gave

$$P = \frac{(0.0411 \pm 0.0005) \times 1.11}{0.465} = 0.097 \pm 0.001$$

- (c) an average asymmetry of events at the upper end of each spectrum over the last 5 MeV energy interval, which gave

$$P = \frac{(0.08 \pm 0.01) \times 1.11}{0.923} = 0.096 \pm 0.012 .$$

All three calibrations were combined to give

$$P = 0.103 \pm 0.009$$

in agreement with the anticipated result.

Displayed in Fig. 17b and 17c are the precession components $S_{Ca} \sin(\omega t + \phi_0)$ extracted from the summed electron data for all electron events and for all electron events throughout the last 5 MeV energy interval of recorded events, respectively.

The computed electron asymmetry α_e^{MC} versus low-energy cut-off is shown in Fig. 19a. The measured electron asymmetry $\alpha_e (= (1.11) \times S_{Ca}/P)$ versus lower energy cut-off is displayed in Fig. 19b. Care must be exercised in making a direct comparison of Figs. 19a to 19b since the gain of the energy scale of the electron data has not been determined.

C. RMC Photon Asymmetry

The time distribution of the summed photon events (Fig. 20a) was analyzed in the same manner as carried out for decay electrons. The variables τ_{Ca} , ω , and ϕ_0 were fixed at the best-fit values to the summed electron data and the carbon term was omitted from the functional form of the time distribution. Neglecting the contribution from carbon is

justified when fitting the spectrum of RMC events only since the relative probability of observing a photon from capture on calcium or carbon in this experiment is $> \Lambda_{\text{Cap}}^{\text{Ca}} / \Lambda_{\text{Cap}}^{\text{C}} \approx 60$. Omission of the carbon term in fitting lower energy regions of the data containing decay electron bremsstrahlung was done for convenience. Retention of this term would not be expected to alter significantly the fitted results of the decay electron bremsstrahlung asymmetry, for which there is little interest.

The time distribution of photon events was then fit to (from Eq. (4))

$$I(t) = A_{\gamma} \exp(-t/\tau_{\text{Ca}}) (1 + S_{\gamma} \sin(\omega t + \phi_0)) + G_{\gamma} ,$$

where A_{γ} and S_{γ} were the only fitted variables and $S_{\gamma} = P\alpha_{\gamma} \times (1.11)^{-1}$. The parameter α_{γ} is the average asymmetry (with respect to the muon spin) of all photons included in the fit. It is the RMC photon asymmetry when all the fitted data lie about 63.5 MeV, α_{γ} is the mean of the RMC asymmetry and the bremsstrahlung asymmetry each appropriately weighted by the relative number of RMC and bremsstrahlung events included in the fit. For each choice of fitted photon energies, G_{γ} was fixed at the observed background ($t < 0$) counts per channel. An upper limit of 82 MeV for accepting photon events was chosen because of a poor signal-to-noise ratio at higher energies. The parameters A_{γ} and S_{γ} were then obtained for several values of the lower NaI channel cut-off.

Results for the measured asymmetry α_γ are given in Table 2 and are graphed along with the measured electron asymmetry in Fig. 21. It is seen that the RMC photon asymmetry and the decay electron asymmetry are of opposite sign. The measured asymmetry of the RMC events above 63.5 MeV was

$$\alpha_\gamma(\geq 63.5 \text{ MeV}) = +0.90 \pm 0.50 \quad .$$

A systematic error of 8% is attached to this result due to the uncertainty in the determination of the residual muon polarization. We display the precession component $S_\gamma \sin(\omega t + \phi_0)$ extracted from the data for all photon events (Fig. 20b) and for the RMC events above 63.5 MeV (Fig. 20c).

It was desirable to check to what extent the measured photon asymmetry is consistent with a mixture of RMC events of a positive asymmetry and electron bremsstrahlung events below 63.5 MeV of a negative asymmetry. An approximation of the number of RMC events in the spectrum below 63.5 MeV was obtained by extrapolating to lower photon energies a fit of the RT theory¹⁰ to the RMC energy spectrum above 63.5 MeV. From a comparison with the actual data below 63.5 MeV, the ratio of RMC to electron bremsstrahlung events in the data above any lower cut-off was calculated. The computed ratios are given in Table 2.

Next, electron bremsstrahlung energy spectra were computed assuming that the emitted bremsstrahlung was accompanied by secondary electrons lacking sufficient energy to escape the target (otherwise, the electron would trigger counter 5 or 6 and veto the photon event).

The residual energy of the secondary electron was specified by a parameter E_{re} (MeV). With the assumption that the bremsstrahlung retains the entire electron asymmetry, the computed bremsstrahlung energy spectrum was folded into the resolution matrix and a determination of the lower energy cut-off dependence of the bremsstrahlung asymmetry was made. For $E_{re} \leq 11$ MeV, the computed average asymmetry of all bremsstrahlung photon energies varied between -0.302 and -0.327 , in reasonable agreement with our measured value of -0.34 ± 0.02 for all photons of energies ≤ 82 MeV (Table 2). Then we write for the measured photon asymmetry α_γ and accompanying error σ_γ :

$$\alpha_\gamma = \frac{\alpha_{RMC} \times N_{RMC} + \alpha_{BREM} \times N_{BREM}}{N_{RMC} + N_{BREM}} = \frac{\alpha_{RMC} \times \frac{N_{RMC}}{N_{BREM}} + \alpha_{BREM}}{1 + \frac{N_{RMC}}{N_{BREM}}}$$

and

$$\sigma_{RMC} = \sigma_\gamma \times \frac{1 + \frac{N_{RMC}}{N_{BREM}}}{\frac{N_{RMC}}{N_{BREM}}} = \sigma_\gamma \times \left[1 + \left(\frac{N_{RMC}}{N_{BREM}} \right)^{-1} \right]$$

For a chosen lower energy cut-off, α_{RMC} and σ_{RMC} are the "extracted" RMC asymmetry and statistical error, α_{BREM} is the computed electron bremsstrahlung asymmetry, and N_{RMC}/N_{BREM} is the computed ratio of RMC events to bremsstrahlung events above the cut-off.

As a specific example, for a cut-off of 49 MeV, α_{BREM} was computed to lie in the interval $-0.935 \leq \alpha_{\text{BREM}} \leq -0.951$ for the reasonable range $1 \text{ MeV} \leq E_{\text{re}} \leq 11 \text{ MeV}$. We then take $\alpha_{\text{BREM}} = -0.943 \pm 0.008$ and use the value of $N_{\text{RMC}}/N_{\text{BREM}}$ from Table 2, to obtain

$$\alpha_{\text{RMC}} \pm \sigma_{\text{RMC}} = +0.76 \pm 0.41$$

"Extracted" values of the RMC asymmetry were consistently $\geq +0.50$, even for cut-offs as low as 37 MeV. However, the computed errors on the "extracted" asymmetry are almost as large as the error on the measured RMC asymmetry at the 63.5 MeV cut-off and should be made even larger since systematic uncertainties arise from incomplete knowledge of the bremsstrahlung spectrum. For this reason we prefer to consider "extracted" values of the RMC asymmetry as only a consistency check and retain the measured RMC asymmetry for the 63.5 MeV cut-off as our final result.

To test the validity of the result obtained for the RMC photon asymmetry, spectra of the functional form $I(t)$ fitted to the photon data were generated in a statistical manner such as to simulate the time distribution of RMC events above 63.5 MeV consistent with the measured amplitude A_{γ} ($= 6.14 \pm 0.2$) and the background level G_{γ} ($= 1.08$). S_{γ} ($= 0.084 \pm 0.046$) was taken to be 0.075 in the simulated data. Approximately 100 spectra were generated and fit by the least-squares program. The values obtained for the fitted parameters A_{γ} and S_{γ} were normally distributed about their "known" values with statistical errors of the same magnitude as observed in the experimental result.

We further checked that the measurement of S_γ for the RMC data peaked at the muon spin precession frequency ω . To check this, A_γ and S_γ were fit at fixed values of ω over the range of $0.01 \leq \omega \leq 0.10$ radians/sec in increments of 0.001 radians/nsec. The measured value of S_γ was a maximum at the muon spin precession frequency. The χ^2 decreased by 4 when ω was fixed within 0.003 radians/nsec of the known frequency. A second decrease in χ^2 was observed at $\omega = 0.057$ radians/nsec but no physical significance was attached to this result since when the analysis was repeated with about 1200 high energy electron events a similar result but with three χ^2 minima was obtained. One minimum χ^2 occurred at the correct frequency; the other two at frequencies different from 0.057 radians/nsec.

D. Expression for the Branching Ratio

The total number of electrons originating from muons which were bound to calcium nuclei and subsequently decayed during the foreground time window was determined to be

$$N_e^{\text{ob}} = (51.49 \pm 0.24) \times 10^6, \quad (6)$$

by a numerical integration of the calcium component of the fit to the summed decay electron time spectra. N_e^{ob} can also be expressed as

$$N_e^{\text{ob}} = N_\mu^{\text{Ca}} \frac{d\Omega}{4\pi} P(1,2,3) P(\text{NaI}) \epsilon_e W_Y \int_{t=137.7\text{nsec}}^{t=783.7\text{nsec}} \exp(-t/\tau_{\text{Ca}}) \Lambda_{\text{Decay}}^{\text{Ca}} dt \quad (7)$$

In Eq. (7)

N_{μ}^{Ca} is the total number of muons that were bound to calcium nuclei. As a first approximation one might take this to be the number of muon stops recorded by the scalers, 4.446×10^{10} .

$\frac{d\Omega}{4\pi}$ is the fractional solid angle between the target and counter 8, determined from a Monte Carlo calculation to be about 0.046.

$P(1,2,3)$ is the probability that an electron event was not accidentally vetoed by a $\overline{1,2,3}$ anticoincidence. An estimate of this is obtained from the scaler ratio $\frac{1,2,3 \cdot 7 \cdot C2 \cdot 8}{7 \cdot C2 \cdot 8}$ (Table 1). However, since this pulse was 30 nsec wide, a fraction $1 - \exp(-30/365)$, or 8%, were not accidental vetoes. Thus, $P(1,2,3) \approx 0.85$.

$P(\text{NaI})$ is the probability that an electron event was not vetoed by the NaI pile-up reject circuit. This was measured to be about 0.88 by removing the rejection circuit and noting the increased electron event rate.

ϵ_e is the efficiency of the counters 5, 6, 7, C2, and 8 for recording electrons. By removing counters 5, 6, 7, and C2 individually from the electron signature it was determined to be ≤ 0.953 , where the equality holds if counter 8 is assumed to be 100% efficient. Unfortunately, counter 8 could not be removed from the signature without affecting the solid

angle $d\Omega/4\pi$, so that it is convenient to define the efficiency ϵ_γ of counters 7, C2, and 8 for detecting converted photon pairs and compute the ratio $\epsilon_\gamma/\epsilon_e$. This was determined to be 1.01 ± 0.01 with no uncertainty due to the efficiency of counter 8. Because converted photons involve two charged particles, and thus an enhanced detection probability, the error 0.01 was computed allowing for the possibility that $\epsilon_\gamma = 1.0$.

W is the probability that an electron did not stop in the matter comprising the target, counters, and 0.30cm lead converter. We measured the electron rate for several thicknesses of lead converter in position and observed that the recorded electron rate increased linearly with decreasing radiation lengths (thickness) of converter. The radiation lengths of the counters were computed and then summed with a Monte Carlo calculation of the average radiations lengths traversed in the target by recorded events. A linear extrapolation of the electron rate to "zero matter" was made. From the result we obtained $W = 0.41 \pm 0.02$. At the conclusion of running, the converter and counters 7 and C2 were physically removed. The measured electron rate in this geometry was consistent with the extrapolation procedure.

Y is the probability that an electron event enters the NaI with sufficient energy to produce a timing pulse. We take

this to be the ratio (e-scint sig·NaI)/(e-scint sig) = 0.94 ± 0.01 as determined from the scaler readings.

$$\int_{t=137.7\text{nsec}}^{t=783.7\text{nsec}} \exp(-t/\tau_{\text{Ca}}) \Lambda_{\text{Decay}}^{\text{Ca}} dt = 0.0936$$

is the probability that a muon bound to a calcium nucleus decays within the foreground time window.

As a check, putting numerical factors in Eq. (7) we obtain $N_e^{\text{ob}} = 52.59 \times 10^5$ (see Eq. (6)).

A similar expression can be written for $N_Y^{\text{ob}}(i)$, the number of background-subtracted RMC events in the i th energy channel of the photon energy spectrum in the foreground time window

$$N_Y^{\text{ob}}(i) = N_{\mu}^{\text{Ca}} \frac{d\Omega}{4\pi} P(1,2,3)P(\text{NaI})\epsilon_Y F \Sigma T(i,j) B(E_j) D(E_j) \int_{137.7\text{nsec}}^{783.7\text{nsec}} \exp(-t/\tau_{\text{Ca}}) \Lambda_{\text{Cap}}^{\text{Ca}} dt \quad (8)$$

The first five terms in this expression have already been discussed. The substitution of $\Lambda_{\text{Cap}}^{\text{Ca}}$ for $\Lambda_{\text{Decay}}^{\text{Ca}}$ has been made so that the integral gives the probability that a muon bound to a calcium nucleus is captured during the foreground time window. Further terms are:

T is the resolution matrix. The j th column of T is the resolution function, normalized to unity, of a photon of initial energy E_j . The first column of T is the resolution of a

10 MeV photon, the second column is the resolution of an 11 MeV photon, and so forth. Thus, the index "j" and the photon energy are related as

$$E_j = (j + 9) \text{ MeV}; j = 1, 2, \dots$$

$D(E_j)$ is the detection probability of a photon of energy E_j (Fig. 13).

$B(E_j)$ is the probability that a muon bound to a calcium nucleus is captured by a proton and a photon of energy E_j to $(E_j + 1)$ MeV is emitted in the process. Thus, $B(E_j)$ represents the differential branching ratio of radiative to normal muon capture in calcium evaluated at E_j and integrated over a 1 MeV interval.

F is the probability that a photon event was not vetoed by an accidental $\overline{5,6}$ pulse, and is ≤ 1.0 . Unfortunately, this factor could not be reliably measured so that we assigned to it a value of 1.0. By examining the scaler value for $\overline{7 \cdot C2 \cdot 8}$ coincidences and the scaler values for $\overline{1,2,3,5,6} \overline{7 \cdot C2 \cdot 8}$ and $\overline{1,2,3} \overline{5 \cdot 6 \cdot 7 \cdot C2 \cdot 8}$ (no 2nd 5·6 cleaning), we determined that all of the $\overline{7 \cdot C2 \cdot 8}$ pulses were apportioned to either photon or electron events so that no large deviation of F from 1.0 is anticipated. Any deviation of F from 1.0 will result in an underestimate of our final result for the branching ratio.

Dividing Eq. (8) by Eq. (7), cancelling common factors, and absorbing $D(E_j)$ into T by matrix multiplication, we obtain

$$N_Y^{ob}(i) = N_e^{ob} \frac{\Lambda_{Cap}^{Ca}}{\Lambda_{Decay}^{Ca}} \frac{\epsilon_Y}{\epsilon_e} \frac{F}{W} \sum_j T(i,j) B(E_j)$$

Upon inserting numerical factors in this expression we obtain

$$N_Y^{ob}(i) = (675.0 \pm 38.0) \times 10^6 \sum_j T(i,j) B(E_j) \quad (9)$$

for which the solution $B(E_j)$ is sought.

E. Branching Ratio of RMC to MC

Equation (9) can be written as

$$N_Y^{ob}(i) = \sum_j T(i,j) B(E_j) \quad (10)$$

with the constant factor absorbed into the matrix T. We now discuss using Eq. (10) to obtain the branching ratio spectrum $B(E_j)$.

$N_Y^{ob}(i)$ was computed by normalizing the background time ($t < 0$) photon energy distribution to the foreground time interval (a factor of 1.686) and subtracting to obtain:

$$N_Y^{ob}(i) = \text{foreground}(i) - 1.686 \times \text{background}(i)$$

The variance σ^2 was defined for each data channel as

$$\sigma^2(i) = \text{foreground}(i) + (1.686)^2 \times \text{background}(i) .$$

For convenience, the data were summed by two channels and the errors combined. An upper energy limit of 89.5 MeV for accepting RMC events for analysis was chosen since no discernible signal was observed at higher energies. Channels $90 \leq i \leq 134$, before summing, correspond to the RMC data in the energy interval between 63.5 MeV and 89.5 MeV. $N_{\gamma}^{\text{ob}}(i)$ and $\sigma_{(i)}^2$, after summing, are presented in Table 3.

An examination of the photon resolution showed that the RMC data above 63.5 MeV depend only on $B(E_j)$ for E_j above 53 MeV. Thus, the RMC data cannot be used to determine the branching ratio spectrum below 53 MeV.

It has been customary in previous experiments^{11,12,36} to extrapolate the fitted branching ratio at the upper end of the photon spectrum to lower photon energies and present the final results for the total branching ratio. However, this makes a direct comparison of the data to different theories and other experimental results difficult.

As an alternative approach we chose to find $B(E_j)$ by two "theory-independent" methods and present final results for the branching ratio spectrum as determined directly from the RMC data above 63.5 MeV. $B(E_j)$ for $E_j \geq 53$ MeV was fit to the data but final results are presented only for $B(E_j)$ above 57 MeV because a component of the decay-electron bremsstrahlung between 53 MeV and 56 MeV may exist.

We present here two "theory-independent" approaches. Both gave identical results for the integrated branching ratio above 57 MeV. A third approach, an attempt to invert T, failed due to the similarity of its adjacent columns.

Method 1 (Unfolding)

A discussion of the algorithm used is given in Appendix 2.

The program sought a general solution B to the matrix equation

$$N_{\gamma}^{ob} = T \times B$$

During successive iterations, computations were made to determine changes in the elements $B(E_j)$ which minimize the difference in number between the observed data N_{γ}^{ob} and the fitted spectrum at each channel of the fitted data. Because $B(E_j)$ was not restricted to the form of an analytic expression, the program could fit the entire data spectrum. With the exception of the first few data channels, a good fit with a normalized χ^2 of 1.0 was made to the data below 90 MeV. The "unfolded" solution for $B(E_j)$ for E_j above 50 MeV is shown in Fig. 22. Note the high energy edge of the decay electron bremsstrahlung spectrum.

A sum of the branching ratio above 57 MeV results in

$$B(\geq 57 \text{ MeV}) = 21.26 \times 10^{-6}$$

The fit to the RMC data in the region (as always) between 63.5 MeV and 89.5 MeV gave $\chi^2 = 22.32$ for 23 channels. No error on B is computed in the unfolding program.

Method 2 (Power Series)

$B(E_j)$ was expanded as an arbitrary power series parameterized by the photon energy E_j . Terms of order E_j^{-3} to E_j^{+3} were allowed with most possible combinations tested.

Several equally good fits were obtained to the RMC data spectrum with different functional forms of $B(E_j)$. The results for a two-parameter best-fit of the form

$$B(E_j) = aE_j^{-2} + bE_j^{-3} ,$$

gave for a sum of the branching ratio above 57 MeV:

$$B(\geq 57 \text{ MeV}) = (21.1 \pm 0.6) \times 10^{-6}$$

and $\chi^2 = 21.41$ for 23 channels.

We have taken the two-parameter fit as our result for the branching ratio spectrum. It is presented in Table 4 for several values of the photon energy and can be computed from

$$10^6 \cdot B(E_j) = \frac{-10658.9}{E_j^2} + \frac{962499.0}{E_j^3} \text{ photons/capture-MeV}$$

$B(E_j)$ is plotted in Fig. 23, with a smooth curve connecting the individual values.

F. Determination of g_p/g_a

The theory of radiative muon capture in ^{10}Ca of Rood, Yano, and Yano¹³ (RYY) was used to express $B(E_j)$ as a function of the parameters k_{max} , ν_{av} , and g_p , all other weak coupling constants being assigned their UFI values.¹³ The parameter k_{max} is the maximum photon energy averaged over final states, ν_{av} , a similarly averaged value of the neutrino energy in normal muon capture, and g_p is the pseudoscalar

coupling constant. The latter was written in terms of the parameter ρ and the four-momentum transfer q at the weak vertex as

$$g_p = \rho g_a \frac{M_\pi^2 + M_\mu^2}{M_\pi^2 - q^2}$$

In the notation of RYY,

$$B(E_j) = N(x; k_{\max}, v_{av}, \rho) dx$$

where

$$x = E_j/k_{\max}$$

$$dx = 1(\text{MeV})/k_{\max}(\text{MeV}),$$

and

$$B(>57\text{MeV}) = \sum_{E_j=57\text{MeV}}^{k_{\max}} B(E_j) = \int_{x=57/k_{\max}}^{x=1} N(x) dx = \frac{\int_{57/k_{\max}}^1 \Lambda_{\text{Rad}}^{\text{Ca}}(x; k_{\max}, \rho)}{\Lambda_{\text{Norm}}^{\text{Ca}}(v_{av}, \rho)} .$$

Calculation of $N(x)$ was quite time-consuming and thus was determined at only one point each 5 MeV interval and then extrapolated linearly between computed points. The theoretical photon momentum-muon spin asymmetry $\alpha_{\text{rnc}}(x)$ was also computed. We present in Fig. 24a the computed photon asymmetry $\alpha_{\text{rnc}}(x)$ and in Fig. 24b the computed differential branching ratio spectrum $N(x)$ for several values of ρ . We also show in Fig. 24a the computed average photon asymmetry that one

would observe experimentally (i.e., taking into account the photon resolution) for each value of ρ and in Fig. 24b the computed integrated branching ratio $B(\geq 57 \text{ MeV})$ for each value of ρ in order to show the sensitivity of the predicted values of these quantities to the magnitude of ρ .

The parameters k_{max} , v_{av} , and ρ were correlated strongly and the statistics of the data did not permit a simultaneous fit to them all. However, a two-parameter fit to the RYY theory¹³ was possible, and thus v_{av} was either fixed or set equal to $k_{\text{max}}/1.02$ (in accordance with Rood and Tolhoek¹⁰ (RT)), and k_{max} and ρ then determined by a least-squares fit.

Results of the least-squares analysis are presented in Table 5. From the best-fit of the RYY theory¹³ to the RMC data above 63.5 MeV we obtained

$$k_{\text{max}} = 86.3 \pm 1.8 \quad (v_{\text{av}} = k_{\text{max}}/1.02)$$

$$\rho = 6.7 \pm 1.5$$

$$\chi^2/\text{fitted channel} = 26.5/23$$

Some approximations made in the theoretical treatment¹³ were valid only at the high-energy end of the photon spectrum ($x \geq 0.5$) and thus an extrapolation of the fitted spectrum to low photon energies in order to compute the total branching ratio was not done. The value for ρ is in good agreement with the Goldberger-Treiman⁴ prediction $g_p \cong +7g_a$.

A two-parameter best-fit of the RT theory¹⁰ to the RMC data above 63.5 MeV gave

$$k_{\max} = 88.4 \pm 1.8 \quad (v_{\text{av}} = k_{\max}/1.02)$$

$$\rho = 0.6 \pm 2.3$$

$$\chi^2/\text{fitted channel} = 24.8/23 \quad .$$

V. DISCUSSION AND CONCLUSIONS

Our result for the photon momentum-muon spin asymmetry 0.90 ± 0.50 is in agreement with the RYY value¹³ of +0.75 and a slightly higher value given by Borchini and deGennaro,¹⁵ both computed for $g_p \approx +7g_a$. The large error of 0.50 does not permit a precise determination of g_p from the asymmetry result. However, our value for the photon asymmetry itself helps to clarify the discrepancy that has existed between theoretical predictions^{10,13,15} of a large positive photon asymmetry and the sole previous measurement¹² which gave a slightly negative value for the photon asymmetry.

The result for the branching ratio is subject to several considerations: (1) a 5.6% (Eq. 9) systematic uncertainty, (2) a possible overestimate of the branching ratio by as much as 8.6% in view of the discrepancy of our measured muon lifetime in calcium with earlier measurements^{11,12,31}, and (3) an underestimate of the branching ratio by an unknown amount since the accidental veto rate of the photon events by the $\overline{5,6}$ anticoincidence is not known.

The "unfolded" branching ratio spectrum shown in Fig. 22, along with the best-fit to the theory of RYY,¹³ contains some interesting information. The events below 53 MeV are dominated by decay electron bremsstrahlung. It is consistent with the bound-muon decay electron energy spectrum³⁵ to attribute the difference of the two

results in the region between 53 and 57 MeV to a high-energy tail of electron bremsstrahlung. We assumed this and then estimated that there were two bremsstrahlung events in the data above 63.5 MeV (a negligible quantity since there are 120 events of 63.5 MeV).

The best-fits of the power series and the "unfolding" methods of the RMC data above 63.5 MeV gave lower χ^2 than the best-fits of the theories of RT^{10} and RYY^{13} . We note the concave appearance of both the power series (Fig. 23) and "unfolded" best-fit branching ratio spectra.

The best-fit of the RT^{10} theory to our data gave $k_{\max} = 88.4 \pm 1.84$ MeV ($\chi^2 = 24.8$), a value consistent with previous measurement^{11,12} in which the experimental results were compared to the RT^{10} theory. The best-fit of RYY^{13} theory to the data gave $k_{\max} = 86.3 \pm 1.85$ MeV ($\chi^2 = 26.5$). Both the poorer χ^2 and the change in k_{\max} can presumably be attributed to the discrepancy among the shapes of the theoretical spectra of RYY^{13} , RT^{10} , and the power series result. The value of ρ (=6.7) of the RYY^{13} best-fit to our data imparts a slight convex shape to the branching ratio spectrum. The best-fit of the RT^{10} theory to our data with $\rho = +0.6$ is more linear. Thus, the lower value of k_{\max} in the RYY^{13} fit is probably a self-consistent compensation in the fitting procedure in order to minimize the effects of the poorer functional form of the fitted branching ratio spectrum.

Since the equivalent of an "unfolded" spectrum has not been presented in the results of earlier experiments^{11,12,35} and since the χ^2 of the RYY^{13} and RT^{10} best-fit branching ratio spectra are not too

poor, there is not sufficient evidence to question the basic functional shape of the theoretical spectrum. A change in this shape would require a substantial modification of the basic theory of RYY.

The normal muon capture rate and the radiative capture rate are computed in the RYY theory¹³ neglecting the nucleon velocity terms.¹⁰ Since the effect¹⁰ of such terms is to increase both the radiative and the normal muon capture rate by about +8%, the branching ratio of RYY¹³ is not affected by the absence of these terms. If we assume that a +8% correction is to be applied to the capture rate calculated in the RYY¹³ theory, we can then obtain $\Lambda_{\text{Cap}}^{\text{Ca}} \approx 49.0 \times 10^5 \text{ sec}^{-1}$ from the RT¹⁰ best fit and $\Lambda_{\text{Cap}}^{\text{Ca}} \approx 39.0 \times 10^5 \text{ sec}^{-1}$ from the RYY¹³ best-fit. The difference in the two results is due to the different fitted values of v_{av} and ρ (each contributing about one-half the difference). Neither of these results is in good agreement with our measured capture rate

$$\Lambda_{\text{Cap}}^{\text{Ca}} = (22.8 \pm 0.6) \times 10^5 \text{ sec}^{-1} .$$

DiLella et al.¹² compared their experimental results for RMC in calcium to the theory of RT¹⁰. They fit their photon energy spectrum above 47 MeV to the predicted branching ratio of RT¹⁰ and then extrapolated their best-fit result to lower photon energies, which gave a total branching ratio of $(1.14 \pm 0.09) \times 10^{-4}$. We assume that their results, as ours, depended strongly on the integrated branching ratio above 57 MeV, which we determined from their best-fit branching ratio spectrum to be 15.4×10^{-6} . A best-fit of the RT¹⁰ theory to our data gave $(20.0 \pm 0.7) \times 10^{-6}$, a factor of 1.3 times their result.

Conversi et al.¹¹ also compared their experimental results for RMC in calcium to the RT^{10} theory. They, too, extrapolated the best-fit of the RT^{10} theory to their data above 60 MeV to lower photon energies. They found a total branching ratio of $(3.1 \pm 0.6) \times 10^{-4}$, roughly twice the value of $(1.51 \pm 0.08) \times 10^{-4}$ determined by an extrapolation of the best-fit of the RT^{10} theory to our data.

It is of interest to assume, as has been proposed,¹² that the result $(3.1 \pm 0.6) \times 10^{-4}$ of Conversi et al.¹¹ is too high by a factor of about 2 due to neutron contamination of their data. A straightforward reduction by 2 of their branching ratio result gives $(1.55 \pm 0.3) \times 10^{-4}$, in agreement with our result of $(1.51 \pm 0.08) \times 10^{-4}$, and in marginal agreement with the result $(1.14 \pm 0.09) \times 10^{-4}$ of diLella et al.¹²

We now make an indirect comparison of our data to two other theories of RMC in ^{40}Ca .

Borchi and deGennero¹⁵ used the Migdal²¹ theory model of the nucleus in their computation. They predict values of $\Lambda_{\text{Rad}}^{\text{Ca}}$ and $\Lambda_{\text{Norm}}^{\text{Ca}}$ each reduced by about 40% with respect to the predictions of RT^{10} for the same values of the weak coupling constants. Consequently, the branching ratio predicted in both theories is the same, all else being equal. Thus a fit of the Borchi and deGennero¹⁵ theory to our data would give a value for ρ ($=g_p/g_a$) similar to that of the best-fit of the RT^{10} theory to our data but with a result for the muon capture rate about 40% lower than the rate predicted by the RT^{10} fit to our data.

Thus, a good fit to our data to the theory of Borchhi and deGennero¹⁵ would be expected to give $g_p \approx + 0.6 g_a$ and $\Lambda_{\text{Cap}}^{\text{Ca}} = 0.6 \times 49 \times 10^5 \text{ sec}^{-1} = 29.4 \times 10^5 \text{ sec}^{-1}$. The result $g_p = 0.6g_a$ is in disagreement with the Goldberger-Treiman⁴ value of $g_p \approx +7g_a$. The computed capture rate in the Borchhi and deGennero¹⁵ theory is in better agreement with our measured capture rate of $(22.8 \pm 0.6) \times 10^5 \text{ sec}^{-1}$ than the best fit of RT¹⁰.

The giant dipole resonance (GDR) model of Fearing¹⁴ is claimed to reduce $\Lambda_{\text{Rad}}^{\text{Ca}}$ by about 40% and the branching ratio by about 20% compared to that of RT¹⁰. This reduction of 20% in the branching ratio is very nearly the reduction in the RYY¹³ theory compared to that of RT¹⁰. Thus, a fit of our data to the GDR model of Fearing¹⁴ would be expected to give the same result for $\rho (=g_p/g_a)$ as did the best-fit to the theory of RYY¹³, i.e., $g_p \approx 6.7 g_a$. However, the result for the muon capture rate would be about 27% lower than the RYY¹³ best-fit result, namely, $\Lambda_{\text{Cap}}^{\text{Ca}} \approx 0.73 \times 39.0 \times 10^5 \text{ sec}^{-1} = 28.5 \times 10^5 \text{ sec}^{-1}$. This "deduced" value of the muon capture rate, as is that of Borchhi and deGennero¹⁵, is in better agreement with our measured rate of $(22.8 \pm 0.6) \times 10^5 \text{ sec}^{-1}$ than that predicted by the best-fit to our data of either the RT¹⁰ theory or the RYY¹³ theory.

TABLE I. SCALER RATES FOR A TYPICAL RMC DATA COLLECTION RUN.

BEAM	BACKWARD μ^-
TARGET	125x125x25 CM ³ TO THE BEAM ⁴⁰ CA
CONVERTER	17.5CM x 17.5CM x 0.30 CM LEAD
PRECESSION MAGNET	109.125 VOLTS 115.21 MV ON SHUNT
TIME	61543 S
I2	13454 M
I2C1	11617 M
I2C13	4177 M
I2C134	1969 M
CLEANED I2C134 STOPS	1108 M
7C28	46184 K
(123)·7C28	35012 K
(123)·(56)·7C28 (NO 2nd 5-6 REJECT)	684 K
γ SCINT SIG (2nd 5-6 REJECT)	615 K
(123)·(56)·7C28 e SCINT SIG	32717 K
γ SCINT SIG+NaI	396 K
e SCINT SIG+NaI	28451 K
μ - γ	37 K
μ -e	2743 K

TABLE 2. RESULTS OF FITTED PHOTON ASYMMETRY. A_γ IS THE AMPLITUDE OF THE DECAYING EXPONENTIAL, G_γ , THE BACKGROUND PER CHANNEL, α_γ , THE ASYMMETRY. S/N DENOTES THE SIGNAL-TO-NOISE AND 'RMC/BREM' IS AN APPROX. RATIO OF RADIATIVE CAPTURE EVENTS TO ELECTRON BREMSSTRAHLUNG EVENTS IN THE FITTED DATA.

ENERGY INTERVAL (MeV)	$A_\gamma \pm \sigma_A$	G_γ	S/N	RMC/BREM	$\alpha_\gamma \pm \sigma_\gamma$
10 - 82	2895 4	256	5.3	.024	-.34 .02
13 "	2235 "	195	5.4	.031	-.41 .03
16 "	1863 "	157	5.6	.036	-.44 .03
19 "	1541 "	128	5.6	.042	-.44 .03
22 "	1250 3	103	5.7	.048	-.45 .04
25 "	984 3	83	5.6	.056	-.47 .04
28 "	751 2	66	5.3	.067	-.47 .04
31 "	550 "	52	5.0	.084	-.44 .05
34 "	383 "	40	4.5	.109	-.42 .07
37 "	254 1	30	4.0	.150	-.40 .08
40 "	161 "	22	3.4	.220	-.37 .11
43 "	96 "	16	2.6	.351	-.26 .14
46 "	52 .6	10.0	2.4	.677	-.10 .19
49 "	34 .5	7.2	2.2	1.154	-.03 .22
51 "	23.6 .4	5.0	2.3	2.00	+.22 .27
53.5 "	17.1 .4	3.5	2.3	3.53	.38 .32
55.5 "	13.2 .3	2.4	2.6	5.72	.41 .34
58.5 "	10.3 .3	1.8	2.7	9.06	.44 .39
60.5 "	7.9 .2	1.4	2.6	17.55	.76 .45
63.5 "	6.1 "	1.08	2.6		.90 .50 ← FINAL RESULTS
65.5 "	4.6 "	0.92	2.3		.46 .60
68.0	3.5 "	0.80	2.0		.71 .70
63.5-70.0	3.84 0.2	0.43	4.2		1.5 .61
" 73.0	4.5 "	0.58	3.7		1.3 .58
" 75.0	5.1 "	0.73	3.3		.89 .56
" 79.5	5.9 "	0.96	2.9		.82 .52
" 84.5	6.3 "	1.21	2.4		1.0 .50
" 89.5	6.5 "	1.38	2.2		1.14 "
" 94.0	" "	1.51	2.0		1.25 "
" 99.0	" "	1.69	1.8		1.26 "

TABLE 3

EXPERIMENTAL PHOTON ENERGY SPECTRUM
SUMMED BY TWO CHANNELS

CHANNELS	FOREGROUND EVENTS	BACK- GROUND EVENTS	F-B EVENTS	σ^2
1 2	66442	10209	56232.55	83653.50
3 4	53930	9306	44624.16	69618.13
5 6	38932	6993	31939.14	50720.86
7 8	32604	5939	26664.79	42616.57
9 10	30019	5292	24727.15	38940.22
11 12	28533	4709	23824.45	36470.87
13 14	26866	4317	22548.56	34144.51
15 16	25889	4016	21873.32	32658.78
17 18	24939	3805	21134.05	31353.52
19 20	23712	3498	20213.88	29609.27
21 22	22556	3218	19337.73	27981.49
23 24	21969	3038	18951.11	27110.39
25 26	20678	2905	17773.30	25574.86
27 28	19518	2662	16856.05	24005.61
29 30	18671	2524	16147.29	22925.56
31 32	17567	2320	15247.28	21477.67
33 34	16191	2156	14034.81	19825.99
35 36	15177	2020	13157.36	18581.79
37 38	13987	1890	12097.17	17172.96
39 40	12890	1647	11242.93	15666.69
41 42	11671	1564	10106.54	14308.43
43 44	10407	1467	8940.32	12879.59
45 46	9224	1268	7936.02	11395.33
47 48	8067	1273	6794.19	10212.75
49 50	7121	1180	5940.91	9110.44
51 52	6189	1027	5162.32	7919.81
53 54	5363	927	4435.79	6926.13
55 56	4528	777	3750.83	5838.19
57 58	3713	757	2956.06	4989.08
59 60	3149	693	2456.12	4317.08
61 62	2617	551	2065.75	3546.35
63 64	2046	573	1472.81	3012.30
65 66	1641	430	1211.11	2365.72
67 68	1345	438	906.68	2083.94
69 70	1111	332	778.89	1670.69
71 72	813	290	523.04	1301.83
73 74	709	268	440.95	1160.89
75 76	537	201	336.38	875.20
77 78	441	152	289.27	696.79
79 80	382	106	275.79	561.05
81 82	324	108	216.11	505.89
83 84	277	72	204.51	399.21
85 86	245	62	182.62	350.16
87 88	202	57	144.68	298.63
89 90	182	29	153.34	230.31
91 92	174	37	136.91	236.53
93 94	139	29	110.34	187.31
95 96	119	24	95.40	158.79
97 98	122	19	103.46	153.26
99 100	112	22	90.08	148.95

TABLE 4. RESULTS FOR THE BRANCHING RATIO B OF RADIATIVE TO NORMAL MUON CAPTURE IN CALCIUM, FROM A BEST FIT ASSUMING A POWER SERIES EXPANSION FOR B. ERRORS ARE TAKEN FROM THE FITTED SPECTRUM B EVALUATED AT THE MAXIMUM PARAMETER VARIATION NECESSARY TO INCREASE THE CHI-SQUARES BY 1.0 COMBINED WITH A 6% SYSTEMATIC ERROR

FROM THE BEST FIT:

$$10^6 \cdot B(E_j) = \frac{-10658.9}{E_j^2} + \frac{962499}{E_j^3}$$

E_j , PHOTON ENERGY (MeV)	$10^6 \cdot B(E_j)$ in PHOTONS PER CAPTURE - MeV	ERROR
57	1.9166	0.16
58	1.7645	
59	1.6244	
60	1.4952	0.12
61	1.3759	
62	1.2657	
63	1.1637	
64	1.0694	
65	.9820	0.07
66	.9009	
67	.8257	
68	.7560	
69	.6911	
70	.6308	0.04
71	.5748	
72	.5226	
73	.4740	
74	.4288	
75	.3866	0.03
76	.3472	
77	.3105	
78	.2763	
79	.2443	
80	.2144	0.02
81	.1865	
82	.1605	
83	.1361	
84	.1133	
85	.0920	0.02
86	.0721	
87	.0534	
88	.0360	
89	.0197	
90	.0044	0.01
91	-0.0099	

TABLE 5. RESULTS OF LEAST SQUARES COMPARISON OF THE EXPERIMENTAL DATA TO THE THEORY OF ROOD, YANO, & YANO. FITTED PARAMETERS ACCOMPANIED WITH ERRORS.

k_{max} (MeV)	$1/\tau_{cv}$ (MeV)	ρ	FITTED ENERGY REGION (MeV)	χ^2 /DATA POINTS	$10^6 \int_{\geq 57.7 MeV} N(x) dx$
81.8 ± 2.1	$k_{max}/1.02$	11.5 ± 1.8	53.5 — 89.5	60/28	22.4
84.4 ± 1.4	"	8.6 ± 1.2	60.5	39/26	21.0
85.2 ± 1.7	"	6.8 ± 1.3	62.5	27/24	19.9
86.3 ± 1.8	"	6.7 ± 1.5	63.5	26/23	19.9
87.4 ± 2.2	"	5.7 ± 1.7	64.5	23/22	19.2
88.0 ± 1.7	"	4.9 ± 1.6	65.5	21/21	13.7
88.2 ± 1.9	"	4.8 ± 1.8	66.5	21/20	18.6
88.8 ± 2.4	"	4.0 ± 2.4	67.5	21/19	18.0
85.9 ± 1.8	90.4	9.5 ± 2.2	63.5	27/23	19.6
86.0 ± 1.8	89.0	8.8 ± 2.2	"	27/23	19.8
86.2 ± 1.9	87.0	7.8 ± 2.3	"	27/23	19.8
86.9 ± 2.3	81.0	4.5 ± 2.3	"	26/23	19.9
91.0	$k_{max}/1.02$	$2.7 \pm .5$	"	31/23	18.6
90.0	"	$3.5 \pm .5$	"	29/23	18.8
89.0	"	$4.4 \pm .4$	"	27/23	19.1
88.0	"	$5.2 \pm .4$	"	26/23	19.3
87.0	"	$6.1 \pm .4$	"	"	19.6
86.0	"	$6.9 \pm .4$	"	"	19.8
85.0	"	$7.7 \pm .4$	"	27/23	20.1

APPENDIX 1

MONTE CARLO PROGRAM

The Monte Carlo program was a computer simulation of the interactions of photons and electrons with components of the experimental geometry as they proceeded from their production in the target into the NaI detector (Fig. 3).

Description of the program

A photon or electron event was assigned a random site in the target and a random outgoing direction. The event was discarded if it would not pass through counter 8. Otherwise, the path lengths of the event through the target, counters, converter, and NaI were computed and expressed in radiation lengths of Ca, C, Na, I, and Pb. Scintillants were taken to be composed of carbon only. The event was passed through each element in turn in steps of a fraction of a radiation length. The step size was 1/50 of a radiation length for all elements, except the NaI, which was subdivided into alternating elements of Na and I each 1/10 of a radiation length.

At each step, all shower components were tested for interaction by bremsstrahlung, pair production, or Compton scattering as applicable to the type of shower component. If the test was positive, the differential probability spectrum (i.e., the probability that a

particle of energy E interacts to produce a secondary particle of energy in the range E' to $E' + dE'$) was computed³⁷ and the secondary particle energy (the photon energy for bremsstrahlung, the e^- energy for pair production, the e^- energy for Compton scattering) chosen in a statistical fashion. Particles created (destroyed) by interactions were then added (subtracted) to the shower. Charged particles also suffered energy loss by ionization at each step.

Photon events were discarded if no charged particle was present in the shower passing through each of counters 7, C2, and 8 or if a charged particle was present in the shower passing through either of counters 5 and 6. Showers initiated by electron events were required to contain at least one charged particle while passing through each of counters 5, 6, 7, C2, and 8. Thus, photon and electron events were required to produce their respective scintillant signatures (Fig. 3).

The kinetic energy of the shower was computed prior to its entering the NaI and again after it had traversed the NaI. The difference in energies was taken to be the amount deposited in the detector. The gain of the NaI energy scale in the Monte Carlo program was set at 0.511 MeV/channel. By coincidence, this was the gain of the experimental NaI energy scale as determined for photon events. Comparison of the Monte Carlo results for electron energy spectra with experimental electron spectra should be done with caution since the calibration was for photons only.

Some approximations were made in the program. Angular scattering following an interaction of a shower component and resolution broadening due to the NaI electronic response were neglected. Neglect of these effects probably accounts for the better resolution of the simulated data contrasted with the experimental data.

The computed photon detection efficiency $D(E_j)$ versus primary photon energy is shown in Fig. 13. $D(E_j)$ was computed as the probability that a photon of energy E_j emerging from the target in a direction such as to pass through counter 8, produced a $\overline{5,6} \cdot 7 \cdot 02 \cdot 8$ coincidence and deposited at least 0.511 MeV of energy in the NaI detector. The computation of $D(E_j)$ was carried out for 0.30cm of lead converter in the simulated geometry. The finite NaI electronic threshold (≤ 6.6 MeV) represented a negligible correction to the results for the photon detection efficiency of photons of energies above 57 MeV.

APPENDIX 2

A METHOD OF OBTAINING A SOLUTION TO $A = B \times C$

Definitions:

A, a vector of length N

B, an N x N matrix

C, a vector of length N

In the context of this work, A_i represents the number of photons observed in the i th energy channel, B is proportional to the matrix of photon resolution functions, and C is the true photon energy spectrum whose solution is desired.

The algorithm begins by making a trial guess for the solution of vector C, which is denoted as C' .

STEP 1 Form the trial fit

$$A'_i = \sum_j B_{i,j} C_j$$

STEP 2 Calculate and store the vector Δ

$$\Delta_i = A_i - A'_i$$

We define ΔC to be the vector added to C' to give a better solution. ΔC is required to satisfy

$$\sum_j \Delta C_j B_{i,j} = \Delta_i \quad (1)$$

and simultaneously

$$\Delta C_j \propto \sum_{\ell} B_{\ell,j} \Delta_{\ell} \equiv K \sum_{\ell} B_{\ell,j} \Delta_{\ell} \quad (2)$$

Equation (1) imposes the condition that the vector ΔC , when added to the present solution vector C' , normalizes the area of the fit spectrum A' to the area of the spectrum A and Eq. (2) states that the relative "goodness" of the magnitude of ΔC_j is proportional to the number of events which ΔC_j can put into each channel ($B_{i,j}$) multiplied by the quantity needed in each channel (Δ_{ℓ}).

We combine Eq. (1) and Eq. (2) to obtain

$$\sum_j B_{i,j} \left\{ K \sum_{\ell} B_{\ell,j} \Delta_{\ell} \right\} = \Delta_i$$

Sum this over i

$$\sum_i \sum_j B_{i,j} K \sum_{\ell} \Delta_{\ell} B_{\ell,j} = \sum_i \Delta_i$$

and solve this for K

$$K = \frac{\sum_i \Delta_i}{\sum_i \sum_j B_{i,j} \sum_{\ell} \Delta_{\ell} B_{\ell,j}} \quad (3)$$

From Eq. (2) and Eq. (3) one obtains

$$\Delta C_j = \frac{\sum_{\ell} \Delta_{\ell} B_{\ell,j} \sum_i \Delta_i}{\sum_i \sum_j B_{i,j} \sum_{\ell} \Delta_{\ell} B_{\ell,j}} \quad (4)$$

In the denominator, the quantity

$$D_j = \sum_i B_{i,j}$$

is a constant vector. It should be calculated once and stored for later use. D_j is proportional to the detection efficiency $D(E_j)$ of a photon of primary energy E_j (Fig. 13).

Equation (4) can be written

$$\Delta C_j = \frac{\sum_{\ell} \Delta_{\ell} B_{\ell,j} \sum_i \Delta_i}{\sum_j D_j \sum_{\ell} \Delta_{\ell} B_{\ell,j}} \quad (5)$$

ΔC_j is to be formed for all j . Then ΔC is added to C' to form a better solution:

$$C'_j \rightarrow C'_j + \Delta C_j$$

This completes the first half of one iteration. Because the areas under the curves of A and A' are now the same, an attempt to repeat the steps up to this point will result in $\Delta C = 0$ since $\sum_i (A_i - A'_i) = 0$ and the numerator of Eq. (3) will vanish. Thus, the iteration is repeated with the replacement

$$\sum_i \Delta_i + \sum_i |\Delta_i|$$

in the numerator of Eq. (5).

STEP 3 Calculate ΔC_j as

$$\Delta C_j = \frac{\sum_{\ell} \Delta_{\ell} B_{\ell,j} \sum_i |\Delta_i|}{\sum_j D_j \sum_{\ell} \Delta_{\ell} B_{\ell,j}}$$

and again

$$C'_j \rightarrow C'_j + \Delta C_j$$

This completes one iteration. Begin next with STEP 1.

Discussion

A. The technique was tested by constructing a spectrum A from $B \times C$ where C was specified by an analytic function, i.e.,

$$C_j = b_0 + b_1 \times j + b_2 \times j^2 + \dots$$

and B was the experimental photon resolution matrix.

The solution C' converged rapidly to C despite a poor initial guess ($C' = 0$).

B. We then took as A the experimental π^- (LiH - Li) data. The "known" solution is a peak at 129.4 MeV and a flat distribution of energies from 55 MeV to 83 MeV. Again, the trial guess was $C' = 0$.

After a considerable number of iterations, a peak and a plateau did appear in the solution C'. However, the solution oscillated in the region between the peak and the plateau in a characteristic Gibbs' phenomenon fashion.

A mathematical proof of the convergence of the algorithm, if one exists, has not been attempted. However, we can examine two classes of problems. First, $A = B \times C$ is exact, as in section A above, and second, $A = B \times C$ is not exact, as in section B. In the first instance, the quantities Δ_i and $|\Delta_i|$ vanish as the solution C' converges to the true solution C. In the second instance $|\Delta_i|$, and thus the solution, will not converge. Since this condition occurs when A_i represents statistical data, one should seek a solution such that $(A_i - A'_i) \approx \pm\sigma_i$, where σ is a measure of the statistical variance of the data. It follows that the quantity $|A_i - A'_i|$ in STEP 3 should be replaced with $|A_i - A'_i| - \sigma_i$. If this is done, a statistically good fit will give

$$\sum_i (A_i - A'_i) \approx \sum_i \{A_i - (A_i \pm \sigma_i)\} = \sum_i \pm \sigma_i \rightarrow 0$$

and

$$\sum_i \{|A_i - A'_i| - \sigma_i\} \approx \sum_i \{|A_i - (A_i \pm \sigma_i)| - \sigma_i\} = \sum_i \{|\pm\sigma_i| - \sigma_i\} \rightarrow 0 \quad ,$$

and the solution will converge.

REFERENCES

1. R. P. Feynman, Phys. Rev. 109, 193 (1958).
2. E. G. Sudarshan and R. E. Marshak, Phys. Rev. 109, 1860 (1958).
3. See, for example, Muon Physics, Vol. II, V. W. Hughes and C. S. Wu, Ed., (Academic Press, New York, 1975) and references therein. For a recent review, see N. C. Mukhopadhyay, Physics Reports 30C, 1 (1977).
4. M. L. Goldberger and S. B. Treiman, Phys. Rev. 111, 354 (1958). For an alternative derivation, see L. Wolfenstein, Phys. Rev. 116, 782 (1959).
5. K. Huang, C. N. Yang, and T. D. Lee, Phys. Rev. 108, 1340 (1957).
6. H. Primakoff, Rev. of Mod. Phys. 31, 802 (1959).
7. R. M. Cantwell, Ph.D. thesis, Washington University (1956).
8. J. Bernstein, Phys. Rev. 115, 694 (1959).
9. G. K. Manacher, Phys. Rev. 116, 782 (1959).
10. H. P. C. Rood and H. A. Tolhoek, Nucl. Phys. 70, 658 (1965).
11. M. Conversi, R. Diebold, and L. diLella, Phys. Rev. B 136, 1077 (1964).
12. L. diLella, I. Hammerman, and L. Rosenstein, Phys. Rev. Lett. 27, 830 (1971); L. M. Rosenstein and I. S. Hammerman, Phys. Rev. C 8, 603 (1973); L. M. Rosenstein, Ph.D. thesis, Nevis-191 (1972) (unpublished).

13. H. P. C. Rood, A. F. Yano, and F. B. Yano, Nucl. Phys. A228, 333 (1974).
14. H. W. Fearing, Phys. Rev. 146, 723 (1966).
15. E. Borchini and S. deGennaro, Phys. Rev. 2, 1012 (1970).
16. P. C. Martin and R. J. Glauber, Phys. Rev. 109, 1307 (1958).
17. A. F. Yano, F. B. Yano, and H. P. C. Rood, Phys. Lett. 37B, 189 (1971).
18. H. P. C. Rood (private communication).
19. J. R. Luyten, H. P. C. Rood, and H. A. Tolhoek, Nucl. Phys. 41, 236 (1963).
20. L. L. Foldy and J. D. Walecka, Nuovo Cimento 34, 1026 (1964).
21. A. B. Migdal, Nucl. Phys. 57, 29 (1964).
22. H. W. Fearing, Phys. Rev. Lett. 35, 79 (1975).
23. The Space Radiation Effects Laboratory is supported by the National Science Foundation, the National Aeronautics and Space Administration, and the Commonwealth of Virginia.
24. M. Eckhause, R. T. Siegel, R. E. Welsh, and T. A. Filippas, Nucl. Phys. 81, 575 (1966), and references therein.
25. R. W. Huff, Ann. of Phys. 16, 288 (1961).
26. M. Chabre, P. Depommier, J. Heintze, and V. Soergel, Phys. Lett. 5, 67 (1963).
27. L. G. Pondrom and A. Strelzoff, Rev. Sci. Instr. 34, 362 (1963).
28. R. M. Sundelin, R. M. Edelstein, A. Suzuki, and K. Tokahashi, Phys. Rev. Lett. 20, 1201 (1968).

29. E. W. Anderson, thesis, Nevis-136 (1965).
30. D. C. Buckle, J. R. Kane, R. T. Siegel, and R. J. Wetmore, Phys. Rev. Lett. 20, 705 (1968).
31. J. C. Sens, Phys. Rev. 113, 679 (1959).
32. J. Duclos, A. Magnon, and J. Picard, Phys. Lett. 47B, 491 (1973).
33. C. S. Hsieh, Ph.D. thesis, College of William and Mary, (1974) (unpublished).
34. See, for example, Muon Physics, Vol. III, V. W. Hughes and C. S. Wu, Ed., (Academic Press, New York, 1975) and references therein.
35. W. R. Johnson, R. F. O'Connell, and C. J. Mullin, Phys. Rev. 124, 904 (1961).
36. W. T. Chu, I. Nadelhaft, and J. Ashkin, Phys. Rev. 137, B352 (1965).
37. B. Rossi, High Energy Physics, (Prentice-Hall, Englewood Cliffs, New Jersey, 1956).

FIGURE CAPTIONS

- Fig. 1 Feynman diagrams of radiative muon capture included in the theoretical study of Rood, Yano, and Yano (Ref. 13). Primed symbols indicate an intermediate state.
- Fig. 2 Experimental meson channel facility of the Space Radiation Effects Laboratory.
- Fig. 3 Side view of the experimental set-up. The counter dimensions and electronic signatures of a muon stop in the target, a photon event and an electron event, are also shown.
- Fig. 4 Beam monitor logic. Circuit output is a good muon stop pulse.
- Fig. 5 Event detection logic. Circuit outputs are the photon and electron scintillant signatures after passing through the "second 5.6" protection logic.
- Fig. 6 Event processing logic. Circuit outputs are the digitized time and energy measurements, which were then recorded on magnetic tape.
- Fig. 7 Observed energy distribution of the photon data accumulated following the muon stop (foreground) and prior to the muon stop (background).
- Fig. 8 Observed energy distribution above 53.5 MeV of the photon data accumulated following the muon stop (foreground) and prior to the muon stop (background). The high energy edge of the decay

electron external bremsstrahlung can be seen in the background distribution.

- Fig. 9 Observed energy distribution of the beam-off (a) photon and (b) electron background.
- Fig. 10 Relative increase of the photon signal with increased thickness of lead converter used.
- Fig. 11 Resolution of the timing logic.
- Fig. 12 Observed energy distribution of photons from π^- captures on protons which materialized in 0.30 cm lead converter. The smooth curve represents a Monte Carlo simulation of the observed photon energy spectrum.
- Fig. 13 Results of a Monte Carlo calculation of the absolute photon detection efficiency versus primary photon energy for 0.30 cm lead converter in position.
- Fig. 14 Observed photon energy distribution from π^- captures on protons. Darkened circles show the best-fit to the data from a study used to obtain the photon resolution function.
- Fig. 15 Photon resolution function.
- Fig. 16 Photon resolution functions for several photon energies.
- Fig. 17 (a) Time distribution with respect to the muon stop ($t = 0$) of a portion of the electron data. (b) The precession component extracted from the electron time spectrum of all electron energies. Error bars do not exceed the dimensions of the data points. The smooth curve is the precession

component $S_{Ca} \sin(\omega \cdot t + \phi_0)$ fitted to the electron time spectrum. (c) Same as (b) but for the electron data above 50 MeV. Data points for (c) were averaged over a half-cycle of the sinusoidal oscillation.

Fig. 18 (a) Monte Carlo calculation of the bound-muon decay electron NaI energy spectrum for 0.30 cm lead converter in position and for no lead converter. (b) Observed decay electron energy spectrum taken with 0.30 cm lead converter in position and for no lead converter. Caution should be exercised in comparing (a) with (b) since the NaI gain was determined for photons only.

Fig. 19 (a) Monte Carlo calculation of the electron asymmetry α_e^{MC} as a function of low energy cut-off. (b) Experimentally measured electron asymmetry α_e versus low channel cut-off of the NaI. Caution should be exercised in comparing (a) with (b) since the NaI gain was determined for photons only. In (b), fitted values of the asymmetry at lower energy cut-offs are not statistically independent of fitted values of the asymmetry at higher cut-offs.

Fig. 20 (a) Time distribution of the photon data with respect to the muon stop ($t = 0$). (b) The precession component extracted from the photon time spectrum of all photon energies below 82 MeV. Error bars do not exceed the dimensions of the data points. The smooth curve is the precession component

$S_{\gamma} \sin(\omega \cdot t + \phi_0)$ fitted to the photon time spectrum.

(c) Same as (b) but for the RMC data in the energy range between 63.5 MeV and 82.0 MeV.

- Fig. 21 Measured asymmetry of the electron and photon data as a function of low channel cut-off for accepting events. The fitted values of the asymmetry at lower energy cut-offs are not statistically independent of fitted values of the asymmetry at higher cut-offs. The RMC photon asymmetry below 63.5 MeV is contaminated by decay electron bremsstrahlung.
- Fig. 22 The branching ratio spectrum as determined after unfolding the photon resolution from the observed photon energy distribution. Also shown is the branching ratio spectrum from the theory of Rood, Yano, and Yano which gave a best-fit to our data.
- Fig. 23 The branching ratio spectrum with the photon resolution removed as determined by an expansion of the branching ratio in an arbitrary power series. Also shown is the branching ratio spectrum from the theory of Rood, Yano, and Yano which gave a best-fit to our data.
- Fig. 24 (a) The predicted photon asymmetry α_{rmc} from the theory of Rood, Yano, and Yano for various values of the pseudoscalar coupling constant g_p ; g_p is related to ρ as $g_p = \rho \frac{M_{\pi}^2 + M_{\mu}^2}{M_{\pi}^2 - q^2} g_a$, where g_a is the axial vector coupling constant and q the 4-momentum transfer. (b) RYY's predicted differential branching ratio spectrum $N(x)$ for various values of g_p .

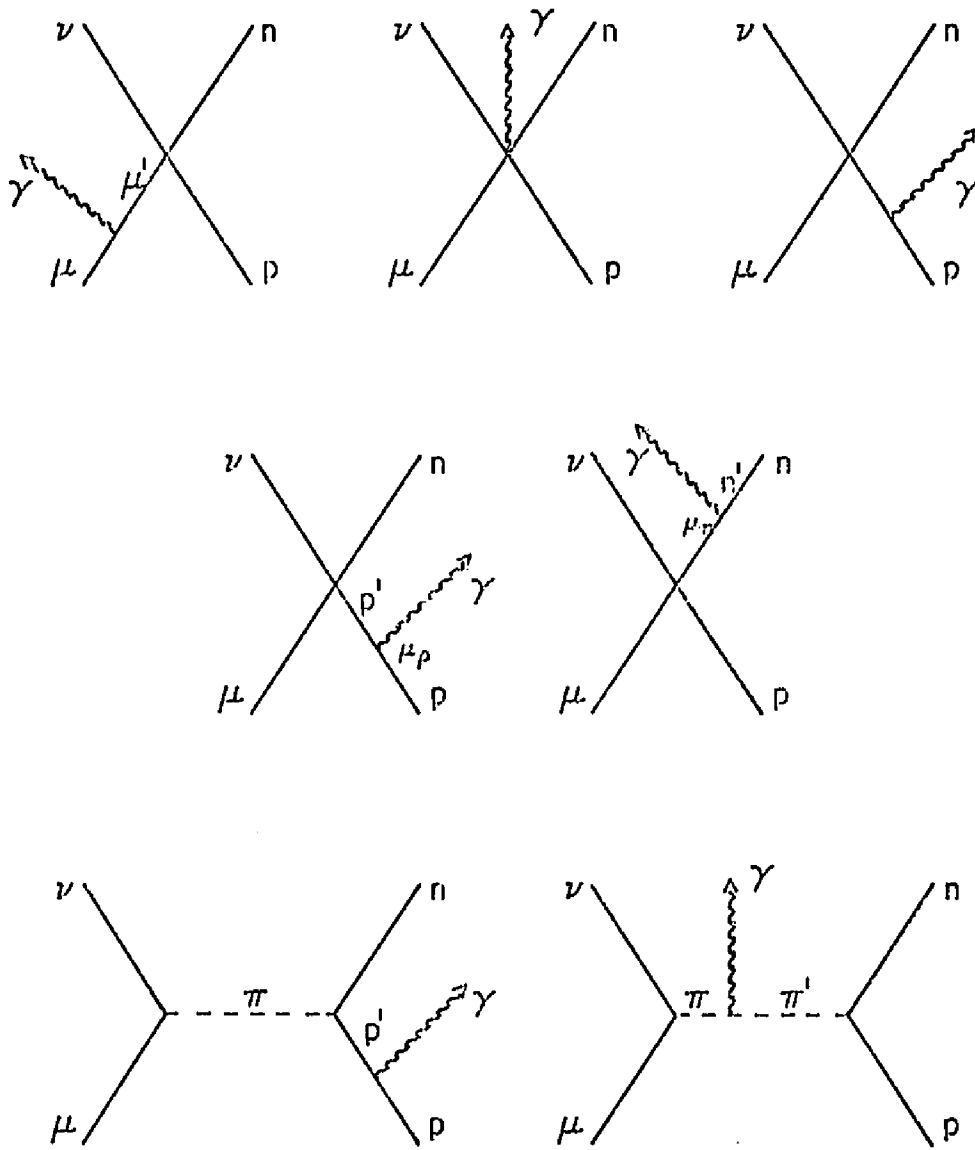


FIG. 1

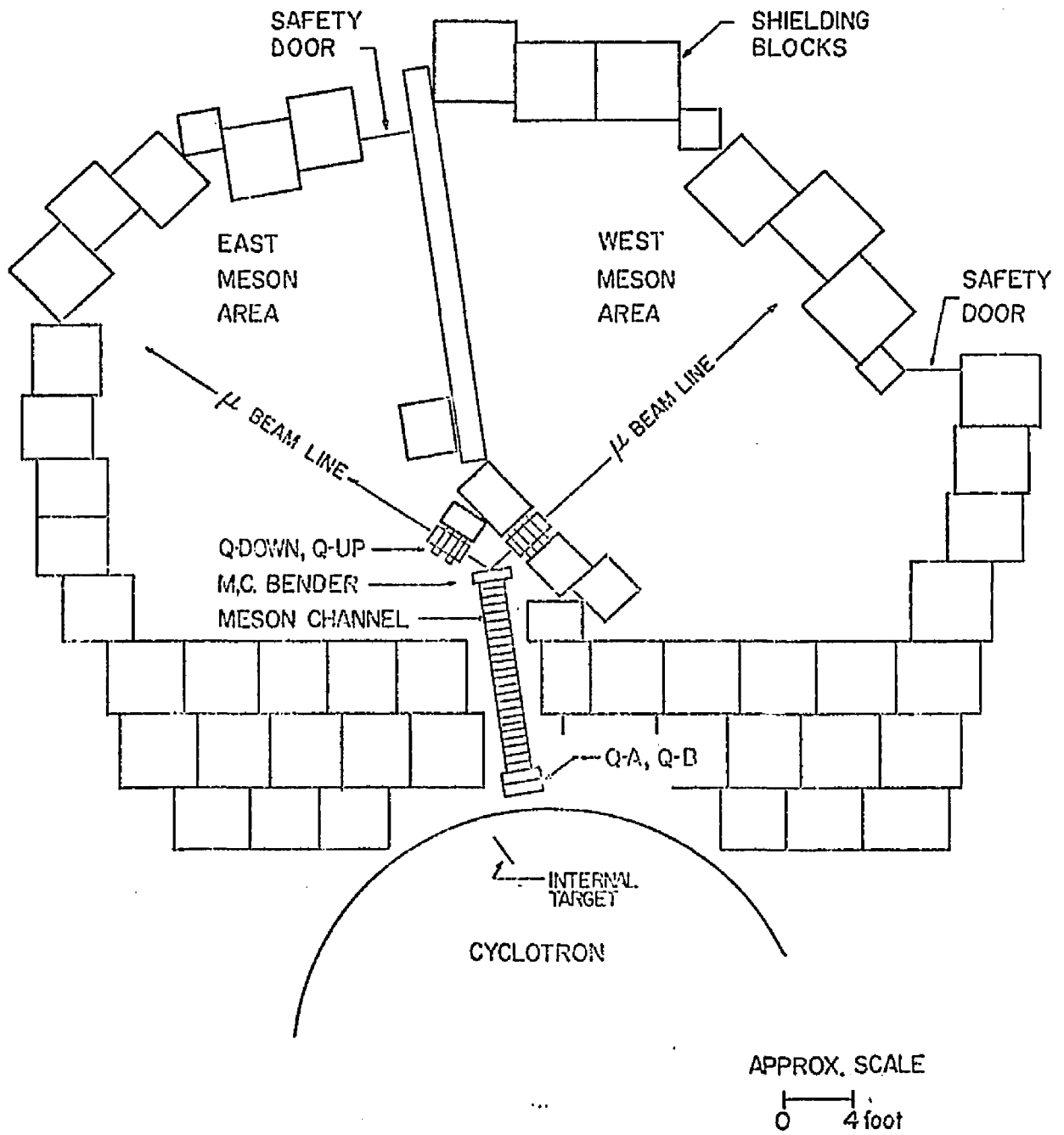


FIG. 2

COUNTER
DIMENSIONS (CM)

Component	Dimensions (CM)	Material
1	30.5 x 30.5 x 1.3	SCINTILLANT
2	25.4 x 25.4 x 0.64	"
3	17.8 x 12.7 x 0.32	"
4	COMPOSED OF 0.64	"
5	25.4 x 25.4 x 0.64	"
6	" " "	"
7	17.8 x 17.8 x 0.64	"
8	15.2 CM DIA. x 0.32	"
C1	20.3 x 20.3 x 1.3	CHERENKOV PLASTIC
C2	17.8 x 17.8 x 1.03	"
Nal	25.4 DIA. x 25.4	Nal (TI)

STOP SIGNATURE:

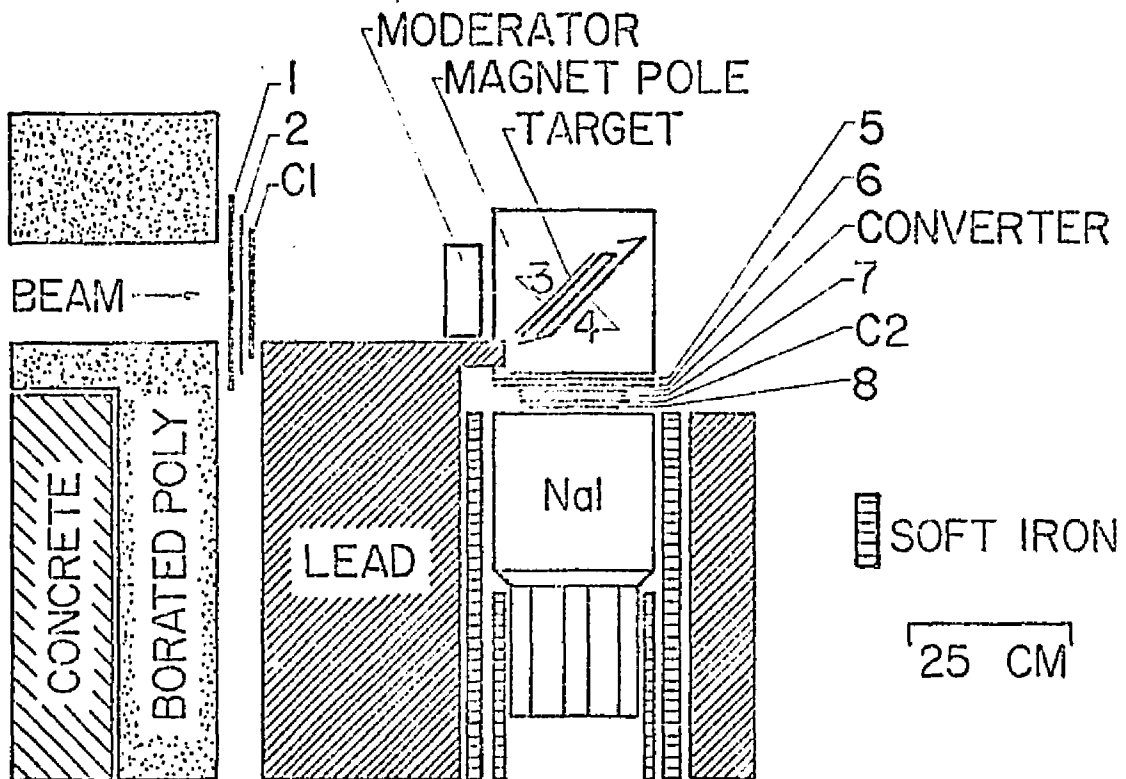
(1-2-C1-3-4) NO 2nd 1-2 IN $\pm 1 \mu\text{sec}$

PHOTON EVENT:

((1,2,3,5,6-7-C2,8) NO 56 IN $\pm 1 \mu\text{sec}$ STOP-Nal*

ELECTRON EVENT:

((1,2,3,5,6-7-C2,8) NO 2nd 56 IN $\pm 1 \mu\text{sec}$ STOP-Nal*



*NaI PULSES WERE REJECTED IF A SECOND PULSE OCCURRED UP TO $4 \mu\text{sec}$ EARLIER OR $1 \mu\text{sec}$ LATER

FIG. 3

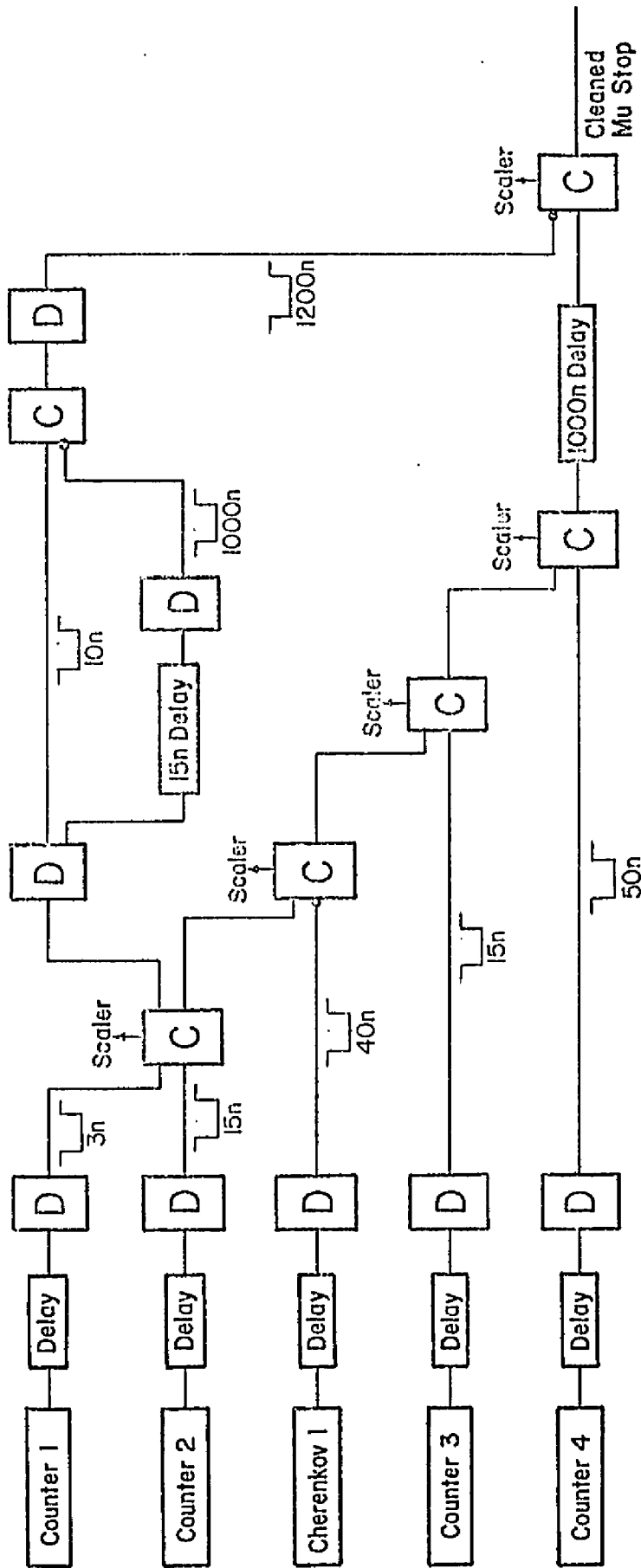


FIG. 4 -

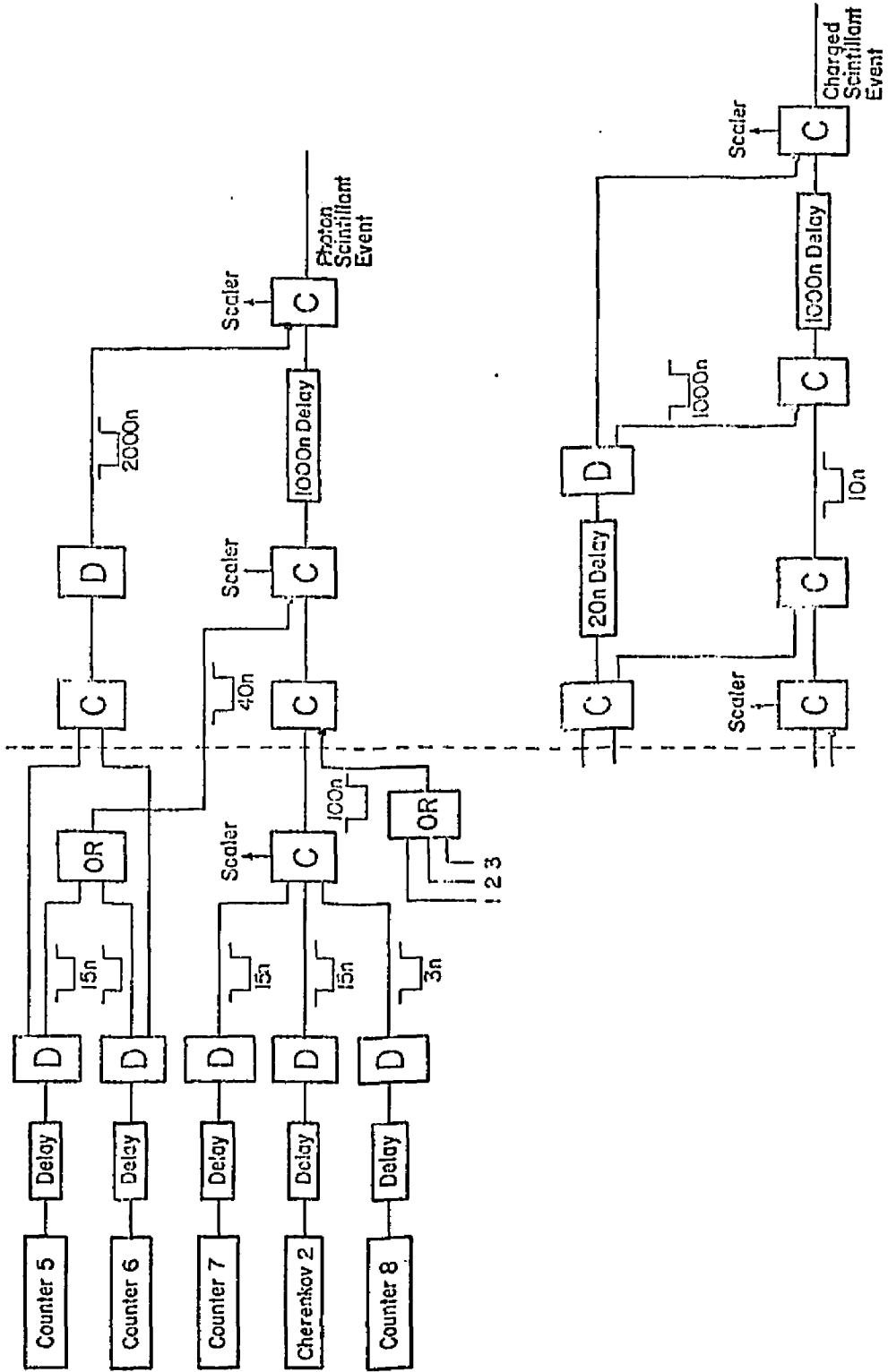


FIG. 5

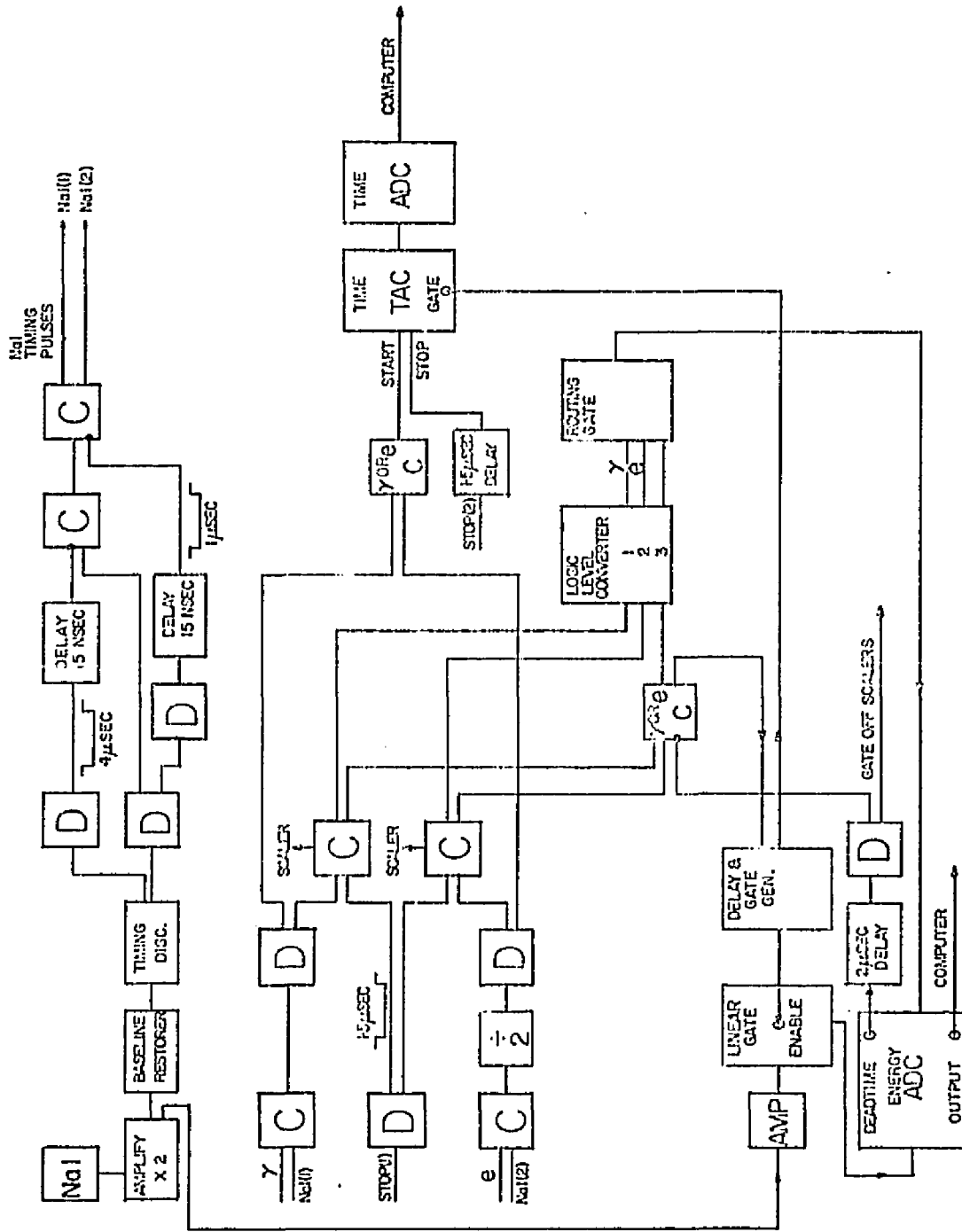


FIG. 6

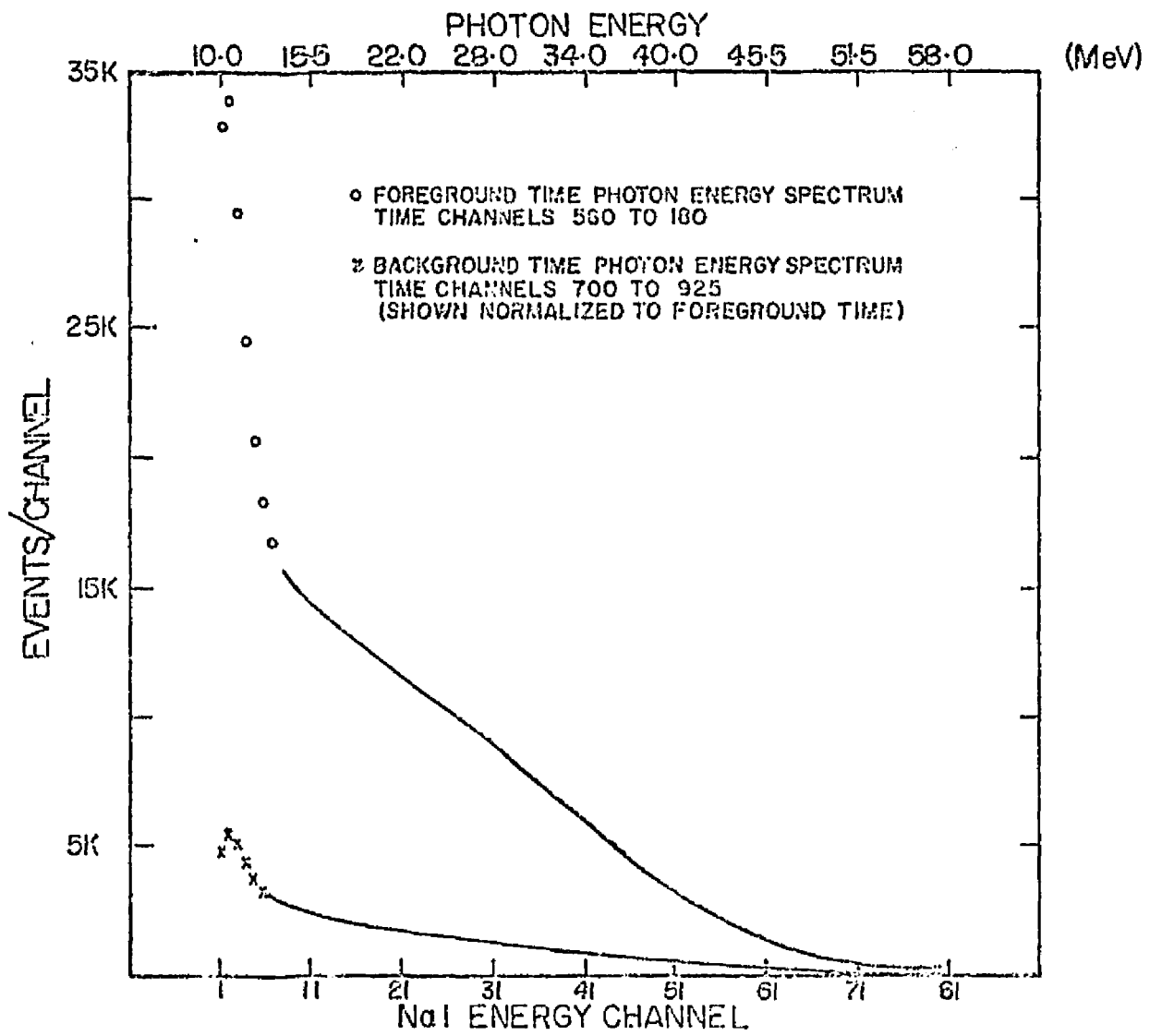


FIG. 7

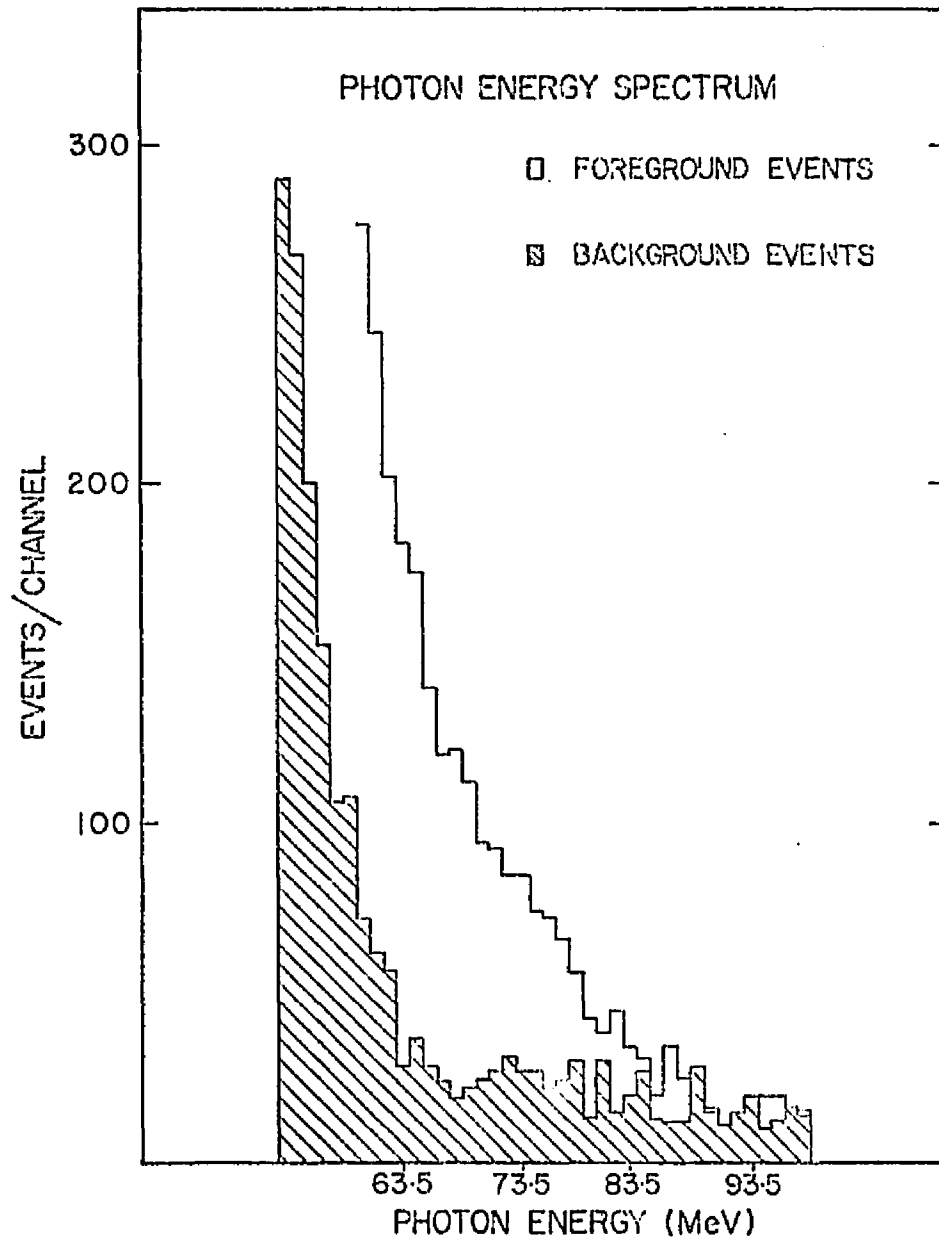


FIG. 8

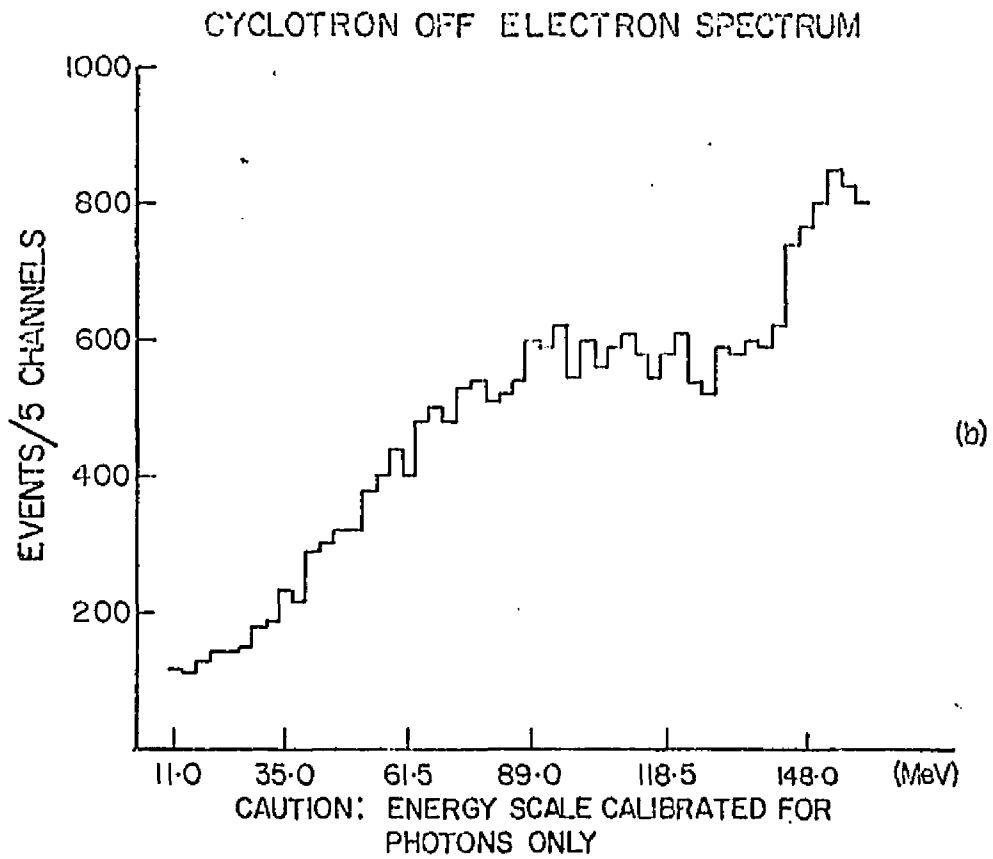
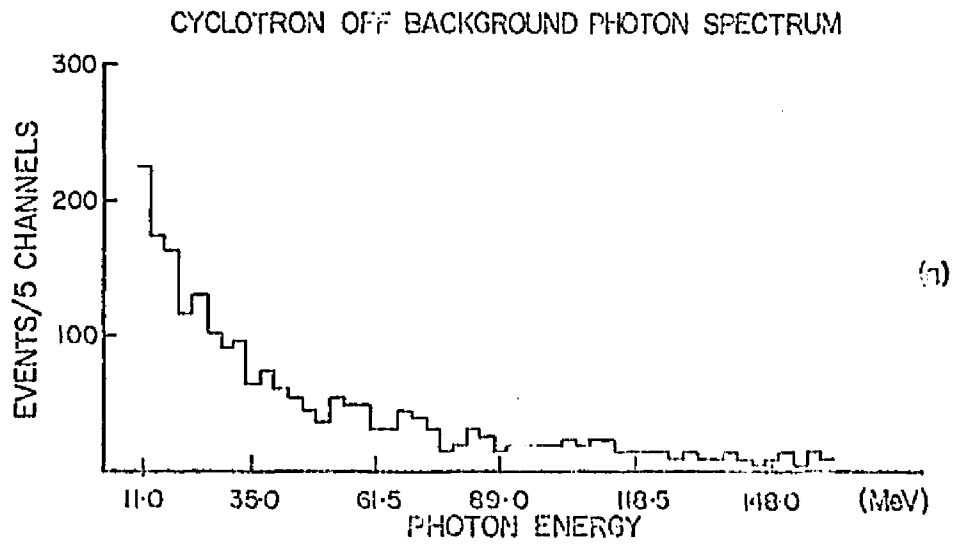


FIG. 9

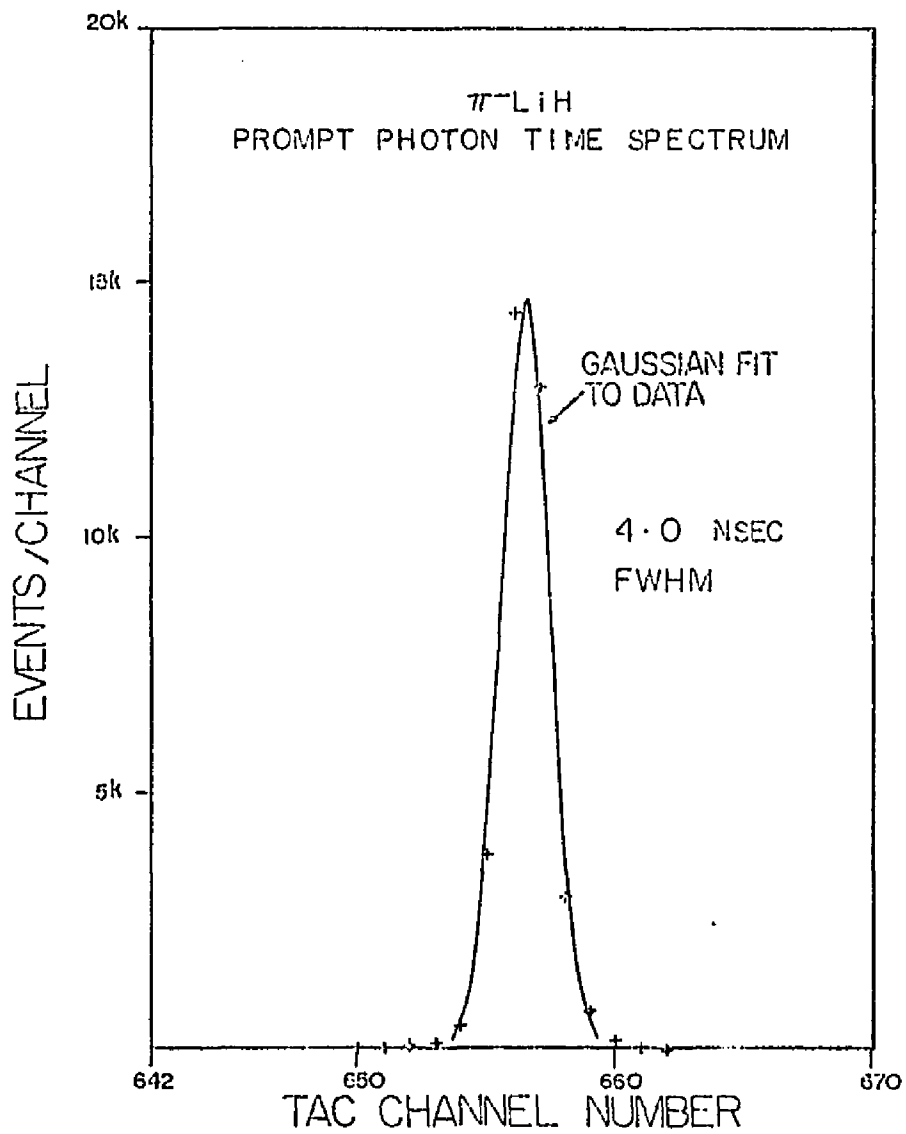


FIG. 11

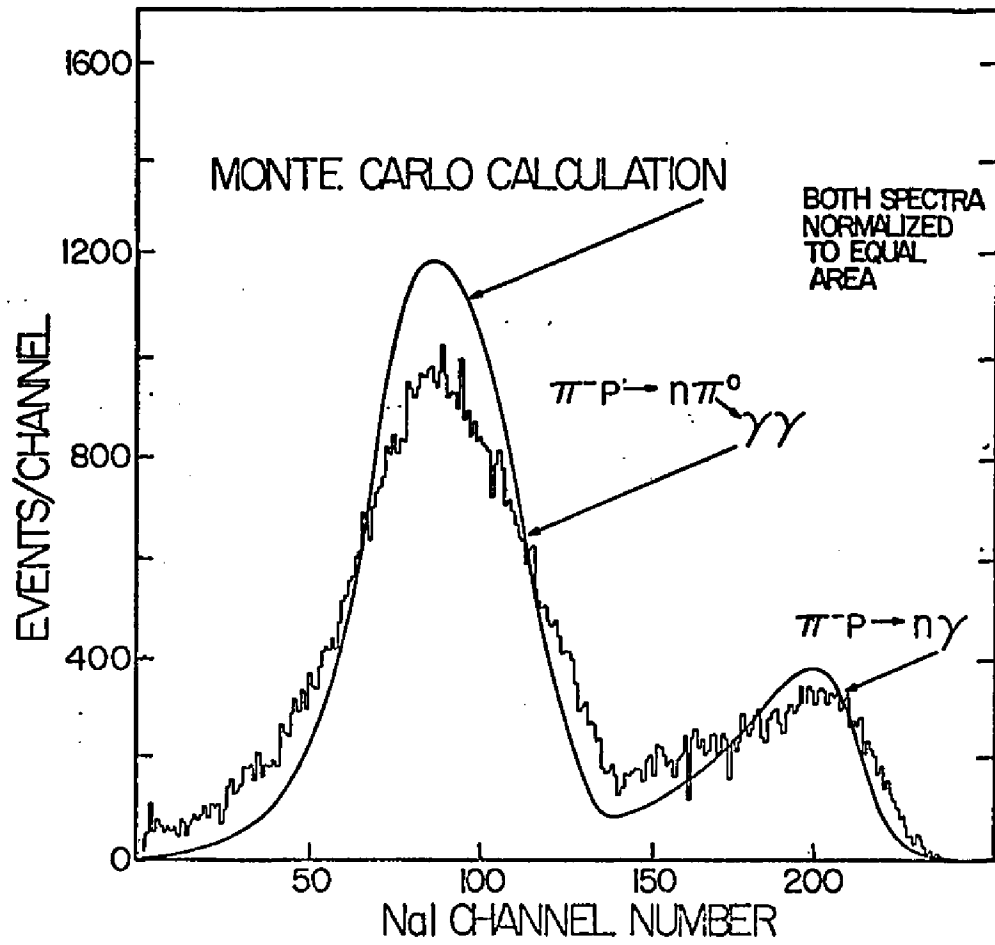


FIG 12

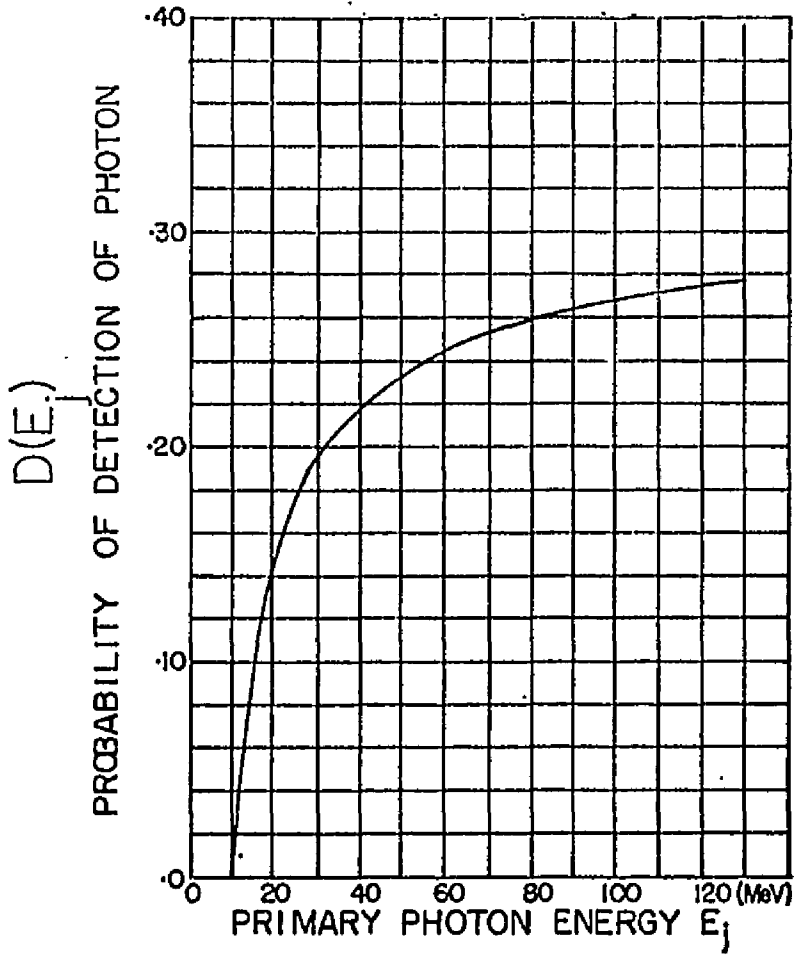


FIG. 13

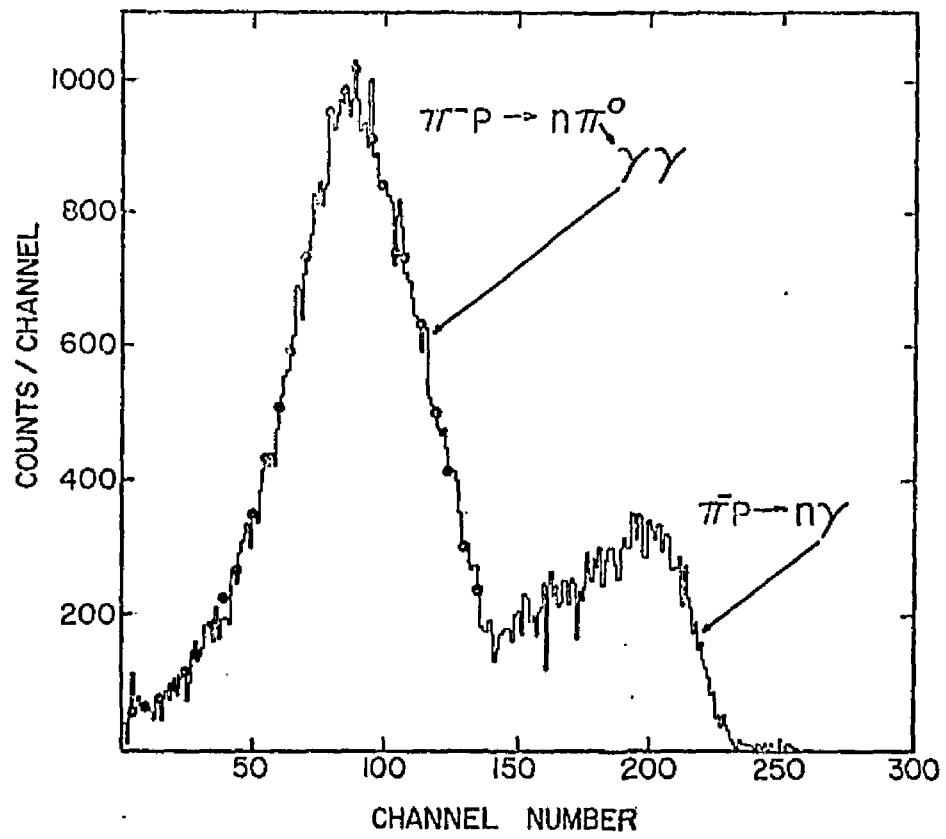


FIG. 14

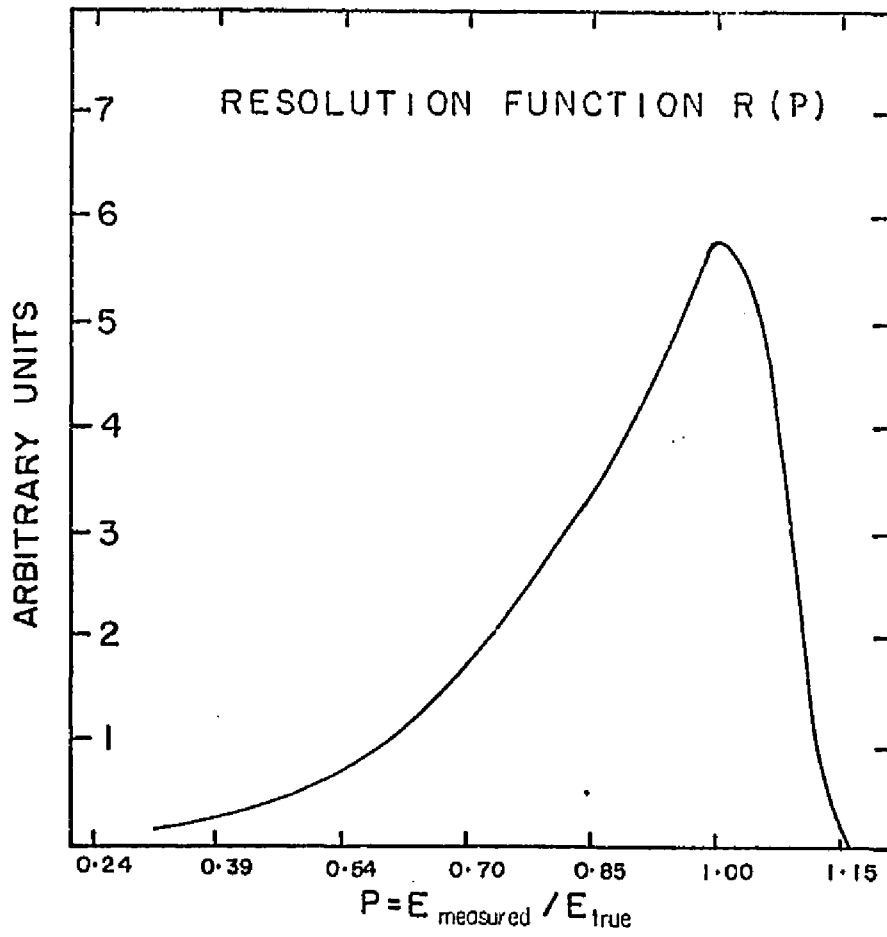


FIG. 15

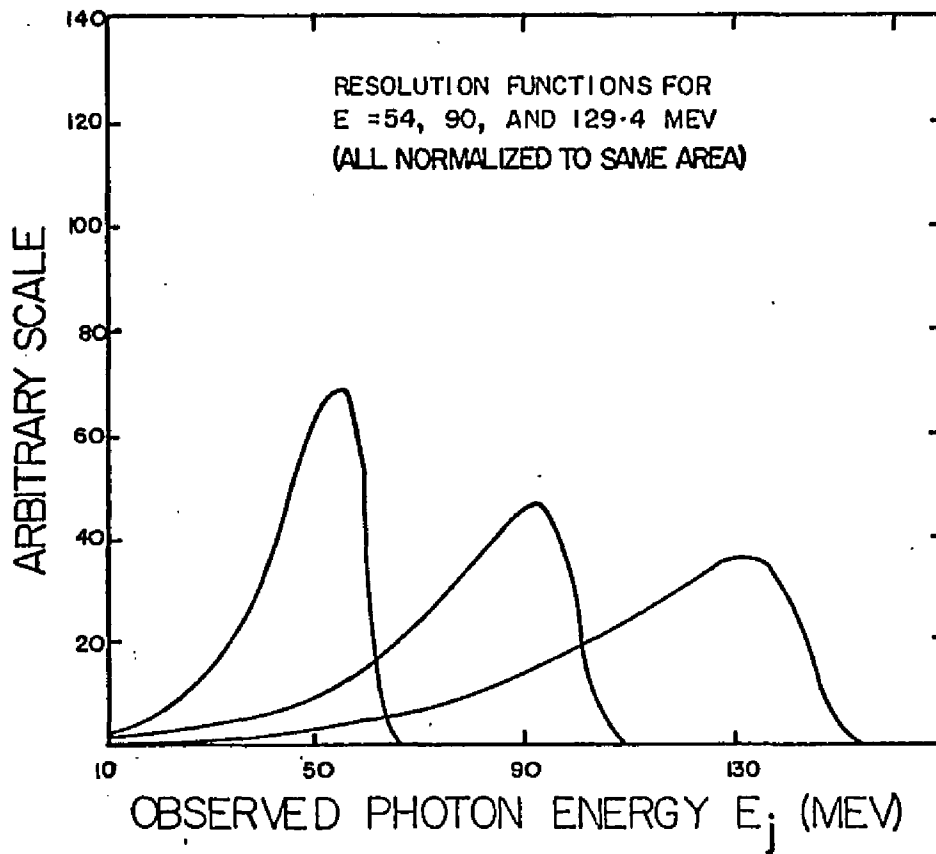


FIG. 16

DECAY ELECTRON DATA

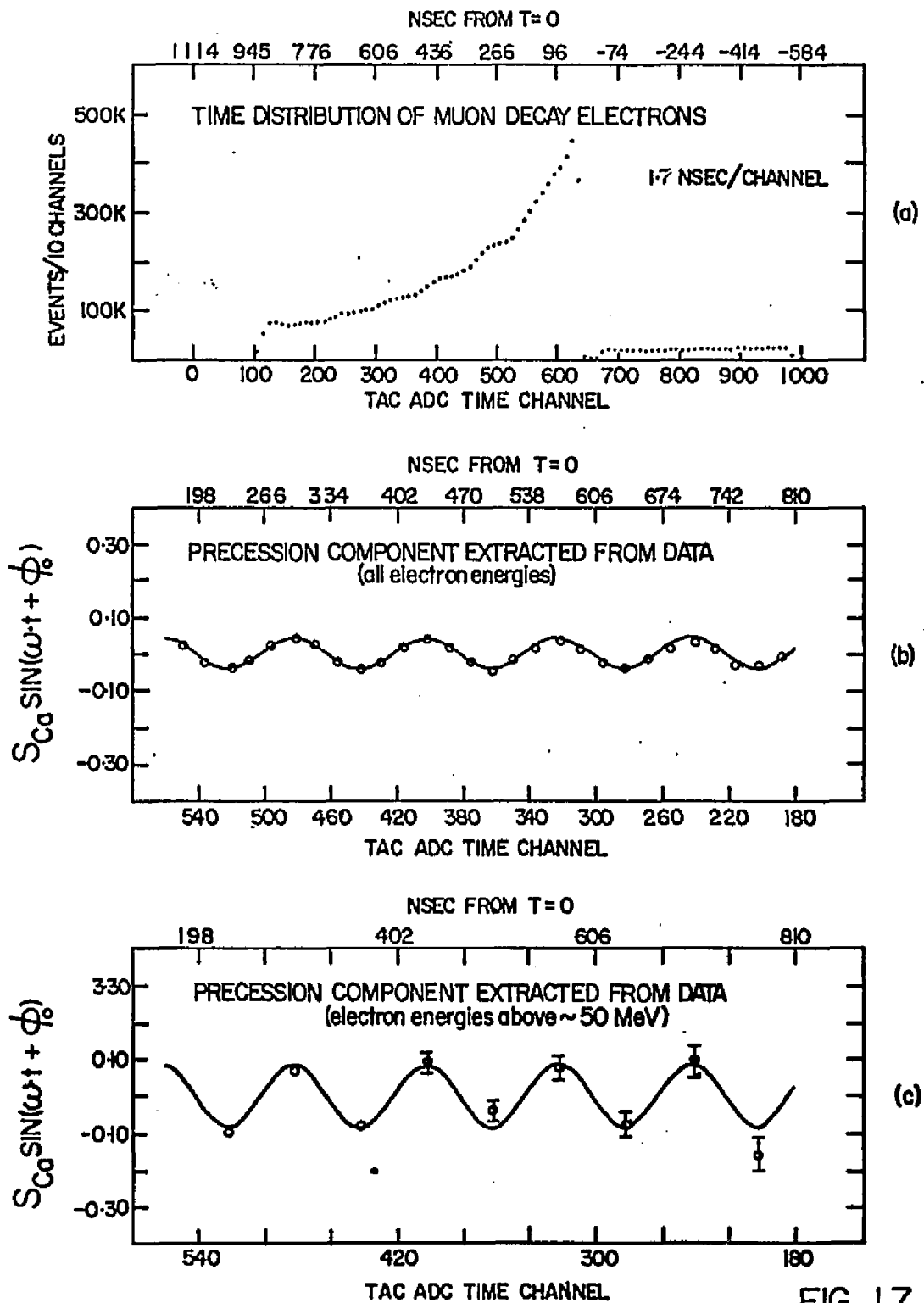


FIG. 17

MONTE CARLO RESULTS OF DECAY ELECTRON ENERGY SPECTRUM

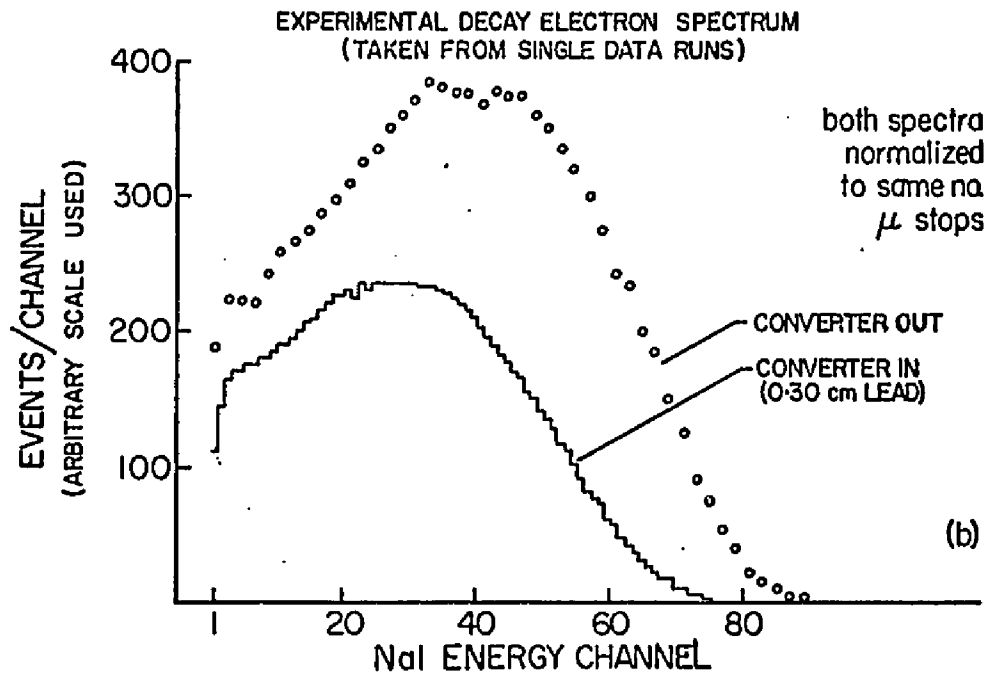
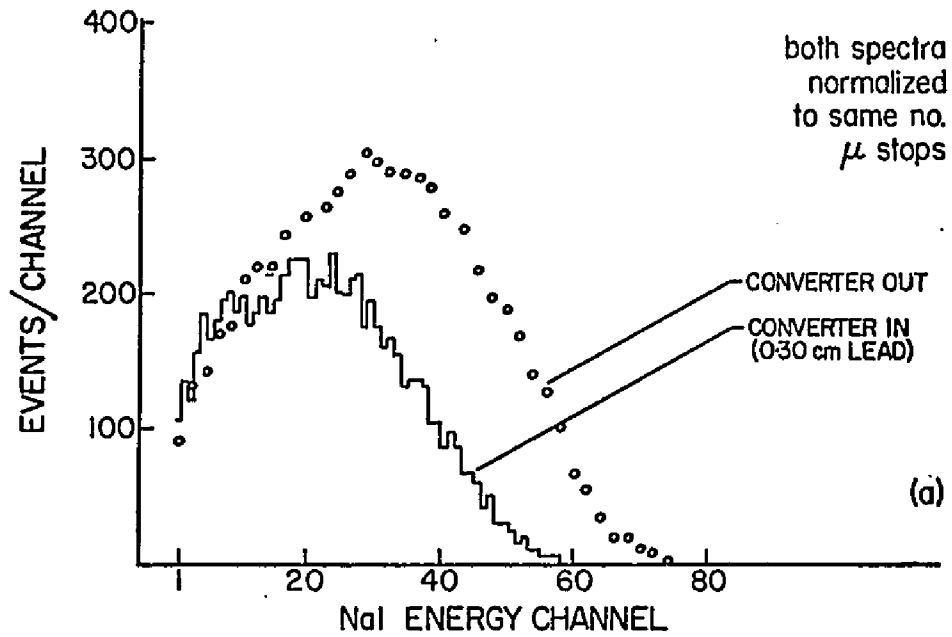
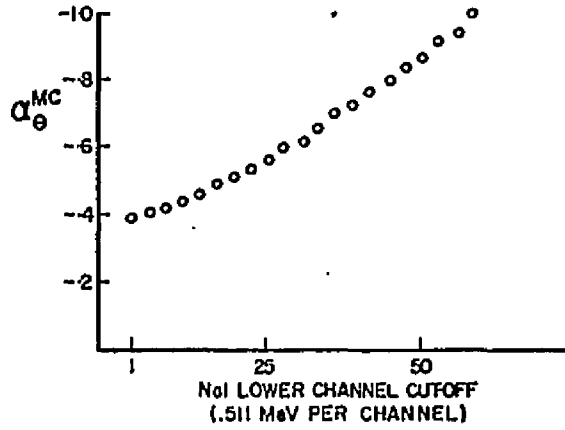


FIG. 18

PREDICTED ELECTRON ASYMMETRY
FROM MONTE CARLO PROGRAM

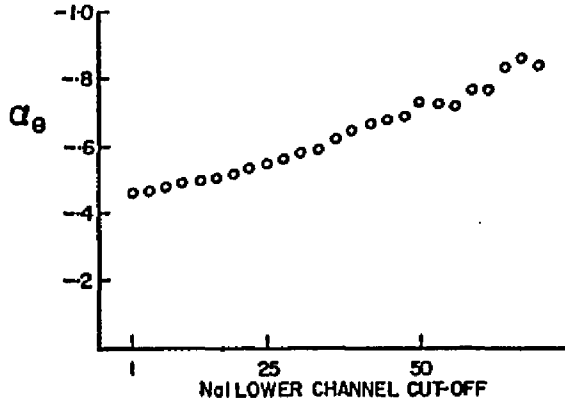
maximum electron energy was channel 63



(a)

EXPERIMENTAL ELECTRON ASYMMETRY
VERSUS LOWER CHANNEL CUT-OFF

maximum electron energy was channel 75



(b)

FIG. 19

PHOTON DATA

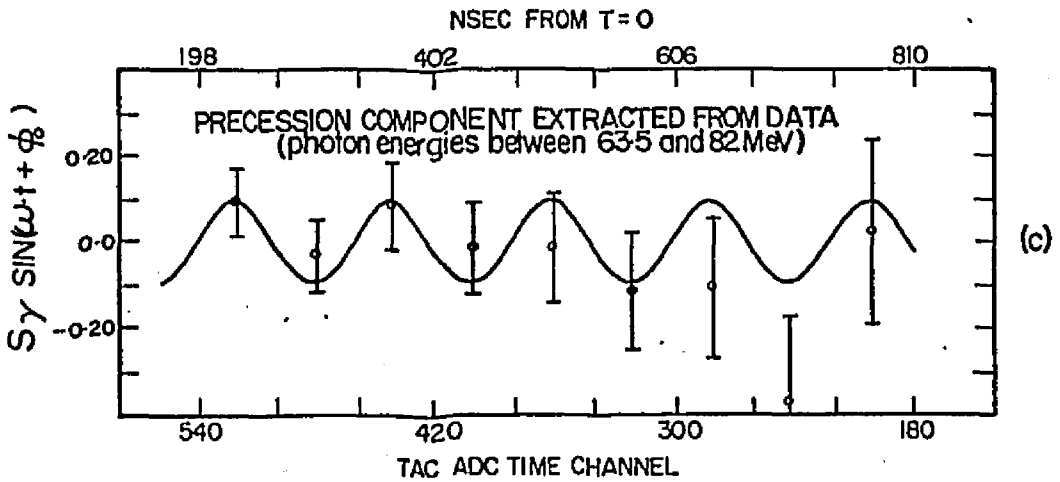
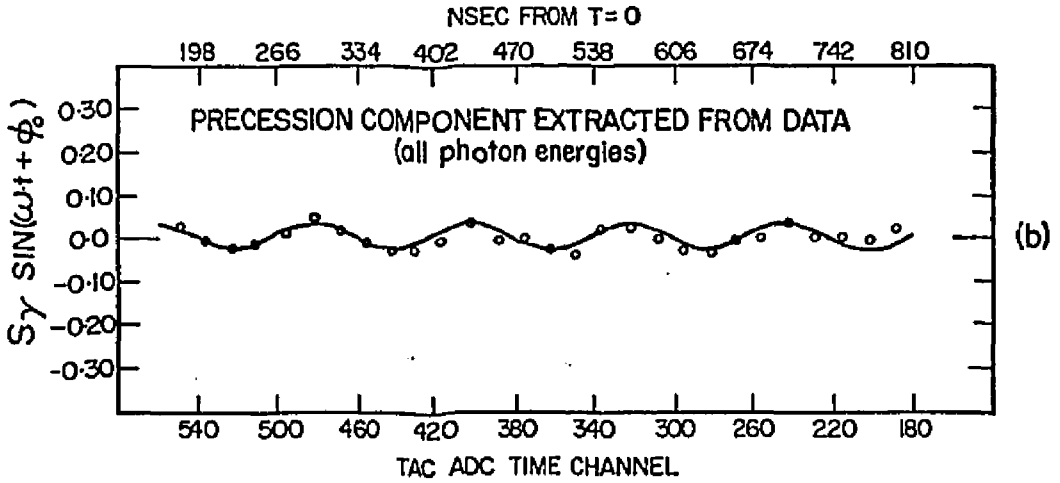
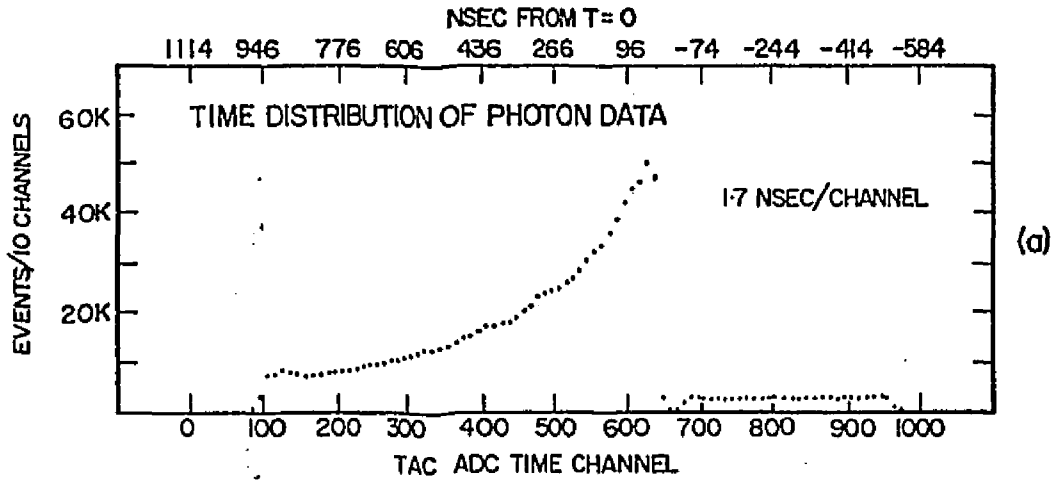


FIG. 20

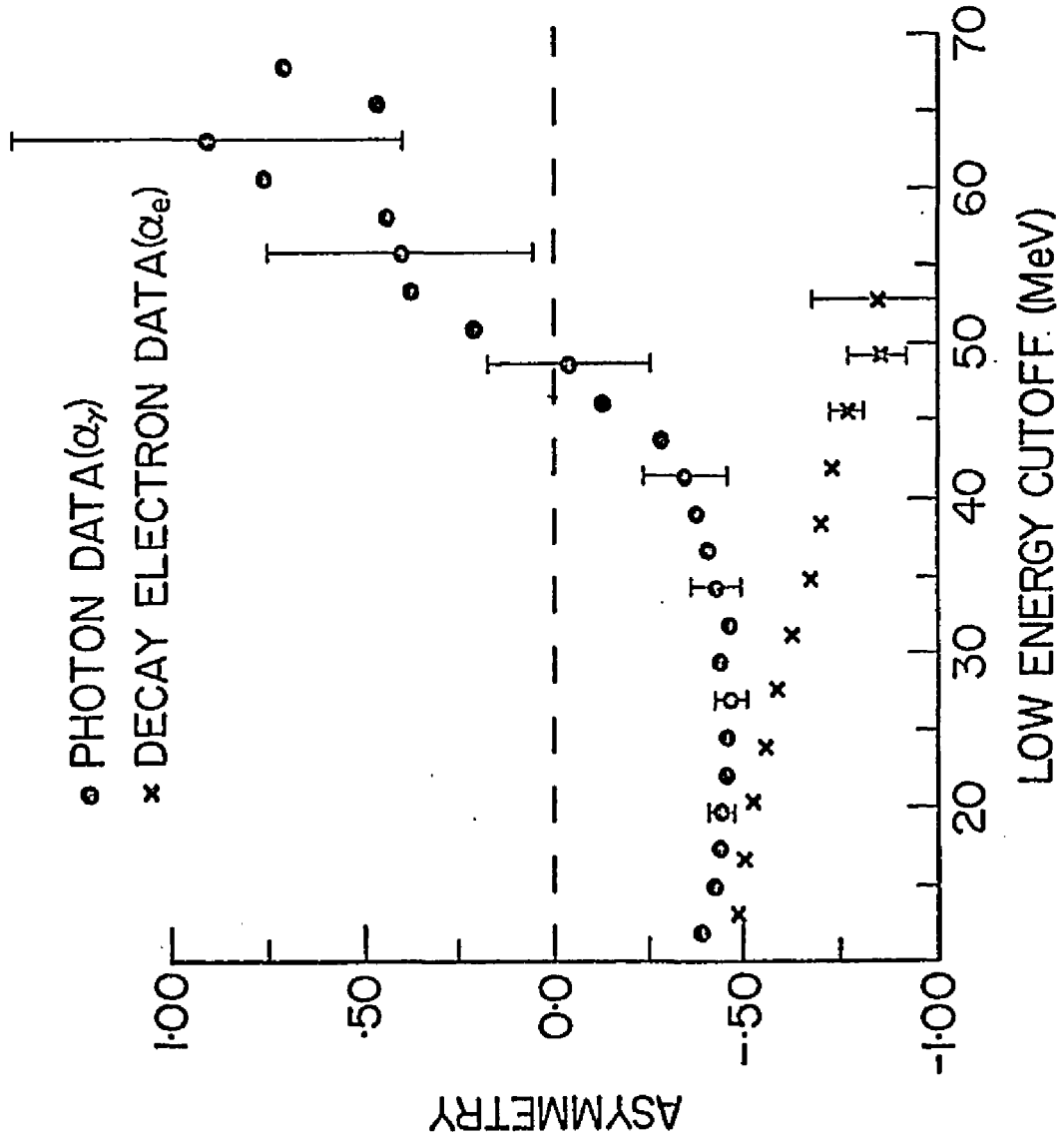
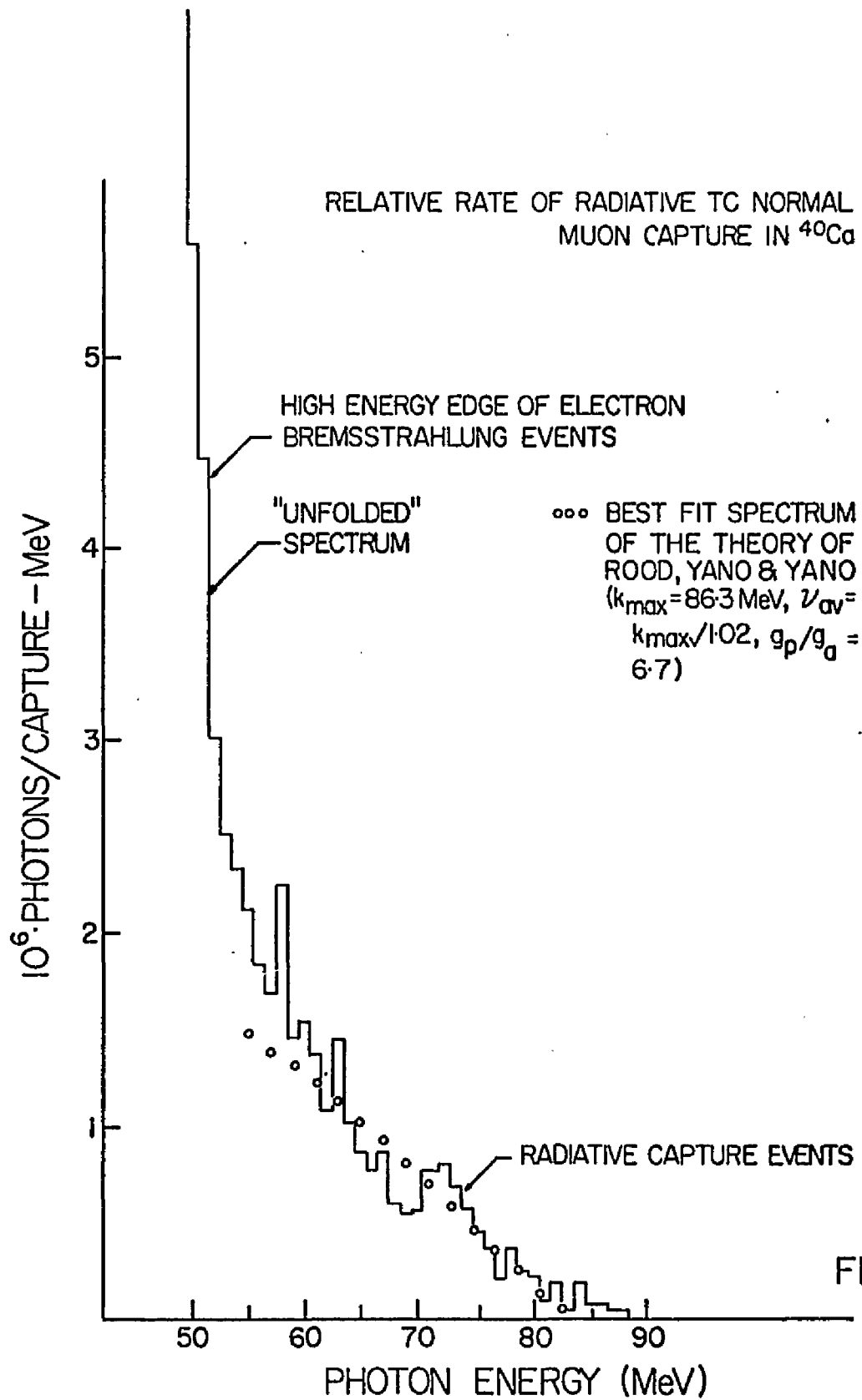


FIG. 21



BRANCHING RATIO OF RADIATIVE TO
NORMAL MUON CAPTURE IN CALCIUM

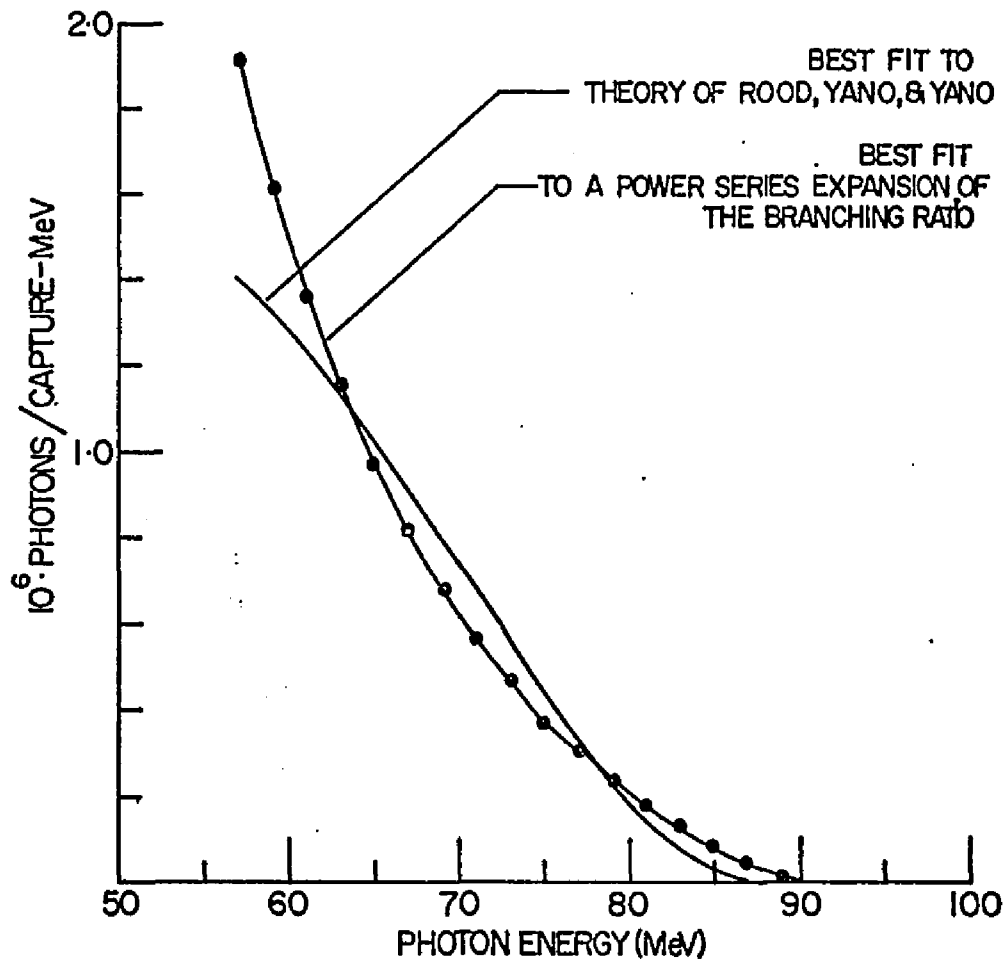
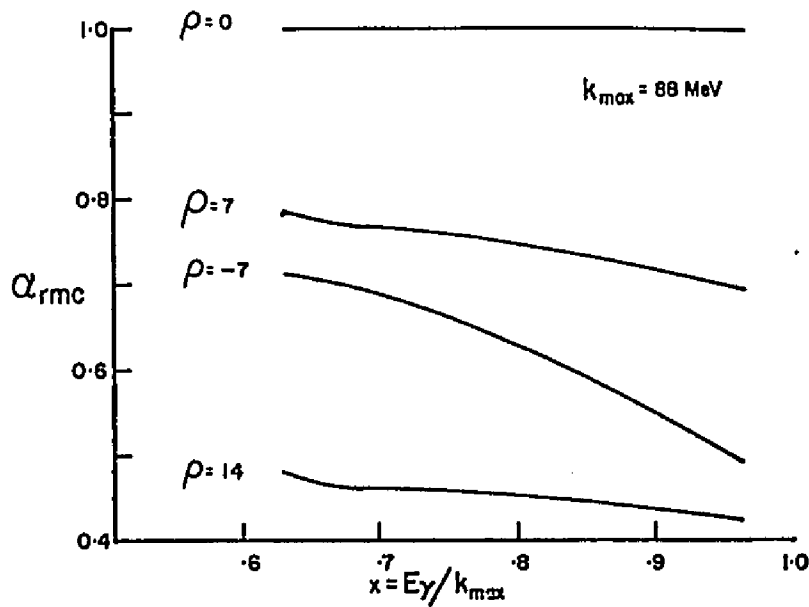


FIG. 23

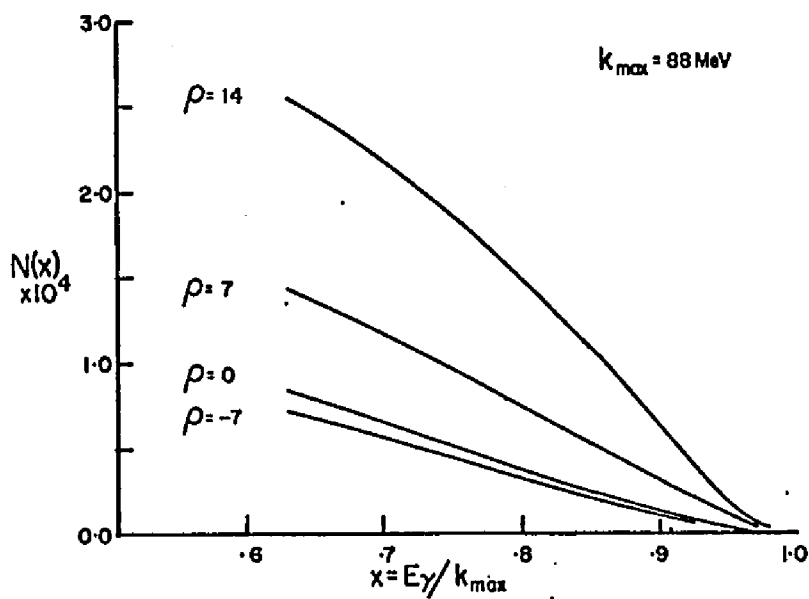
PHOTON ANGULAR ASYMMETRY
(THEORY OF ROOD, YANO, YANO)



ρ	AVERAGE ASYMMETRY ABOVE 63.5 MeV
14	+0.451
7	0.744
0	1.00
-7	+0.624

(a)

DIFFERENTIAL
BRANCHING RATIO SPECTRUM
(THEORY OF ROOD, YANO, YANO)



ρ	$10^6 \int N(x) dx \geq 57 \text{ MeV}$
14	44.82
7	23.02
0	12.43
-7	10.73

(b)

FIG. 24